NTNU – Trondheim
Norwegian University of
Science and Technology

Mesoscale gravity wave activity in the Mesosphere over Northern-Norway

Erlend Magnus Tjelle

Teacher Education with Master of Science
Submission date: July 2014
Supervisor: Patrick Joseph Espy, IFY

Norwegian University of Science and Technology
Department of Physics

Acknowledgement

A huge thank you to my supervisor, Patrick Joseph Espy. Throughout this prolonged semester you have always been available to me, either via mail or good talks at your office. You have filled me with knowledge and motivation whenever needed.
You are truly an inspiration. Thank you for being you!

Next, I want to thank Nora Kleinknecht for introducing me to the curve fitting tool in Matlab, and for being helpful with other Matlab problems.
I also want to thank my parents, for always supporting me and cheering me on. And an extra thanks to my dad, for checking my spelling.
Finally, I need to thank my little brother and my soon to be sister in law, for making my time in Trondheim be about more than just physics. I'm looking forward to your wedding this Saturday (best timing ever)!

Abstract

The purpose of this study is to examine wind data retrieved from the SKiYMET-radars at Trondheim and Andenes during the time period of the 27th of November to the 02nd of December 2012. These dates surrounds the night between the 29th-30th of November, were Hennum (2013) discovered large scale fluctuations in the hydroxyl layer due to gravity wave activity over Trondheim. Similar fluctuations where found over Andenes (although not mentioned in Hennum's thesis), providing for the possibility of a mesoscale connected gravity wave system with wavefronts stretching over 700 km in the middle atmosphere.

The analyses of the wind data results in a significant correlation for the mean zonal and meridional anomalies over Andenes and Trondheim. Further, balloon soundings during the period show that the Scandinavian mountain range does not seem to be the source, but rather a large scale moving frontal wave system, or shear waves.

Målet med denne studien er å utforske vindmålinger knyttet opp mot datoene 27. november til 2. desember, 2012, hentet fra SKiYMET-radarene som er plassert i Trondheim og på Andenes. Disse datoene omringer natten mellom den 29. og 30. november, hvor Hennum (2013) oppdaget store svingninger i hydroxyl "airglow" laget, grunnet bølgeaktivitet i mesosfæren over Trondheim. Lignende svingninger ble oppdaget over Andenes (men ble ikke nevnt i Hennums master oppgave), noe som kan tyde på en utstrekt bølgeaktivitet på mesoskala med bølgefronter som strekker seg 700 km i atmosfæren.

Analysen av vindmålingene resulterer i en signifikant korrelasjon for de gjennomsnittlige "vest-øst" vindene og "nord-sør" vindene mellom Andenes og Trondheim, etter at de større vindsystemene "tidal waves" er fjernet fra datasettene. Videre viser målinger fra værballonger at den skandinaviske fjellkjeden sannsynligvis ikke er kilden til dette store bølgesystemet. Det er heller mer tenkelig at bølgesystemet har oppstått etter en vekselsvirkning av et stort frontal system forflytter seg i troposfæren.

Contents

Chapter 1

Introduction

If the conditions are right, gravity waves created in the troposphere will propagate upwards in the atmosphere and carry momentum and energy with them. As energy is conserved, gravity waves will grow in amplitude as they climb in altitude where the neutral density decreases. This may lead to waves in the mesosphere with amplitudes of several meters per seconds. When they dissipates, they have effectively contributed to a transfer of energy and momentum in the atmosphere. The energy transfers may be of the scale that can alter the mean flow at the dissipation region.
These actions may trouble the weather forecasts if their computer models does not account for the making and breaking of gravity waves. Having realized this, meteorologists are now putting a lot of effort in improving their meteorological models with proper parametrizations of gravity wave activities. (Hocking, 2001).

Gravity waves can be observed in a number of ways; from observing lenticular clouds related to mountain waves (important for airplane pilots), to more sophisticated methods as to measuring perturbations of the hydroxyl (OH) layer with airglow spectrometry and by tracking motions of ionized particles dissolved from incoming meteors with meteor radars. In this study, the last two methods are applied. The SKiYMET-radars, and Andor Shamrock spectrographs located at Trondheim ($63.24°N, 10.27°E$) and Andenes ($69.17°N, 16.00°E$) are used to observe gravity waves in the mesosphere.
Although gravity waves are a well known phenomenon, one may discuss how large in scale they can grow. During the night between the 29th and 30th of November in 2012, Hennum (2013) discovered gravity wave activity above Trondheim due to perturbations in the OH airglow layer. He also observed similar perturbations in the OH layer above Andenes, but did not include these findings in his thesis. Could these oscillations be connected somehow? A mesoscale gravity wave system with wavefronts stretching from Trondheim to Andenes?
There would in any case be needed a mesoscale source to the wave, and the Scandinavian mountain range seems as a plausible source.

Chapter 2

Theory

2.1 The Atmosphere

The atmosphere is commonly divided into vertical layers. If we consider the first 100 km of our atmosphere, these layers are called the troposphere (0 km - 15 km), stratosphere (20 km - 42 km), mesosphere (50 km - 90 km) and the thermosphere (>95 km). These separations are based upon how the atmospheric temperature varies with altitude. In the troposphere and mesosphere the temperature decreases with height, while it increases in the regions of the stratosphere and thermosphere. Between these layers we find approximately isothermal regions, called the tropopause, stratopause and mesopause. (fig 2.1).

The heating of the stratosphere relates to the photochemical processes between oxygen and ultraviolet radiation ($h\nu$) taking place during the making of ozone (O_3)

$$O_2 + h\nu \rightarrow 2O \tag{2.1}$$

$$O + O_2 \rightarrow O_3 \tag{2.2}$$

and the splitting of ozone (Andrews, 2010).

$$O_3 + h\nu \rightarrow O + O_2 \tag{2.3}$$

In the thermosphere, heating is caused by dissociation and ionization of O_2 and N_2 (Berge, 2011). The excess photon energy in the dissociation process is carried away as kinetic energy by the products and causes the temperature to increase.

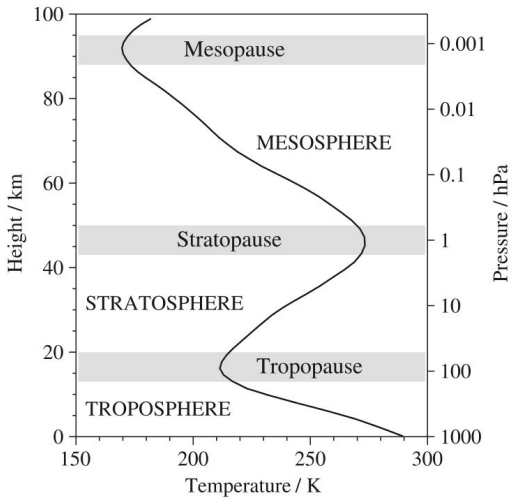

Figure 2.1: Layers of the atmosphere (Andrews, 2010)

2.2 The physics of our Atmosphere

Good approximations and assumptions are important to describe and understand our atmosphere. In thermodynamics, the ideal gas law (below) describes the relationships between a gas's pressure, volume and temperature. This law will be most accurate when describing a monoatomic gas at high temperatures and low pressures.

$$pV_m = RT \tag{2.4}$$

here, p is the pressure, V_m is the volume of one mole, R is the universal gas constant and T is the absolute temperature. By recognizing that $\rho = M_m/V_m$, one can derive the ideal gas law based on air density (ρ):

$$\begin{aligned} \frac{pV_m}{M_m} &= \frac{RT}{M_m} \\ p &= R_a T \rho \end{aligned} \tag{2.5}$$

where $R_a \equiv \frac{R}{M_m}$ is the gas constant per unit mass of air.

Even though the atmosphere mainly consists of a mixture of the diatomic gasses (N_2 and O_2), the approximation of it obeying the ideal gas law is robust. (Andrews, 2010)

Next, an assumption of static equilibrium in the atmosphere is made. Meaning that the forces acting upon a parcel of air cancel each other out. When at rest, the only forces acting on an air parcel are gravity and pressure forces. For simplicity, we consider the parcel to have a cylindrical shape of height Δz and cross-section area ΔA. This parcel

will feel two forces pressing it down, a pressure force acting on the top of the cylinder $F_{top} = p(z + \Delta z)\Delta A$, and the gravitational force $F_g = g\Delta m$, where $\Delta m = \rho \Delta A \Delta z$ and g is the gravitational acceleration. The pressure force acting on the bottom $F_{bottom} = pz\Delta A$, pressing the parcel upward, must then be equally strong as the sum of these. This gives us:

$$\begin{aligned} F_{bottom} &= F_{top} + F_g \\ pz\Delta A &= p(z + \Delta z)\Delta A + g\Delta m \end{aligned} \tag{2.6}$$

Which, by cancelling ΔA and using Taylor expansion, gives us the equation for hydrostatic balance:

$$\frac{dp}{dz} = -g\rho \tag{2.7}$$

In other words, the pressure will always decrease with height for an atmosphere in statistic equlibrium.

As figure 2.1 shows, the temperature of the atmosphere fluctuates with altitude. The rate of decrease of temperature with height is defined by the lapse rate Γ:

$$\Gamma = -\frac{dT}{dz} \tag{2.8}$$

The lapse rate will later be used to define whether or not our atmosphere is stable.

Waves in the atmosphere are much like ocean waves. When propagating through the atmosphere, they will move parcels of air up and down, causing them to oscillate. But the parcels will only oscillate in a stable atmosphere.
Parcels which are moved adiabatically upwards by a wave, will not follow the lapse rate defined for the surrounding environment. Their temperatures will depend on an adiabatic lapse rate Γ_a, which denotes the rate of decrease in temperature inside the air parcels. If $\Gamma_a > \Gamma$, the parcels will reach a point where they are colder and denser than the surrounding air, and hence fall back down where they came from, and start to oscillate (fig. 2.4). This denotes a stable atmosphere (Andrews, 2010).
If however $\Gamma_a < \Gamma$, the air parcel will always be warmer and lighter than its surrounding air, causing it to accelerate upwards instead of oscillating. This denotes an unstable atmosphere, where oscillating parcels of air (and gravity waves), cannot exist (Hocking, 2001).

2.3 Wave systems - Origins and behaviour

The phenomenon *wind* is driven by pressure differences in the atmosphere. Since pressure difference is equivalent to a force per unit area, air in and between high- and low-pressure states will feel a driving force, and winds will arise in order to even out the difference in pressure.

To find one cause of these pressure differences, we can examine the ideal gas law (eq. 2.4). Here it is shown that the local pressure is closely related to the local absolute temperature. It turns out that differential heating of the atmosphere creates the origin of tidal waves, which will be described below.

2.3.1 Atmospheric tidal waves

Thermally driven tidal waves are a well known observed phenomenon in our atmosphere. As discussed above, atmospheric heating depends on the composition of gasses at different layers of the atmosphere. Due to the heating induced as gasses like ozone absorb solar photons, the atmosphere in this region expands and gives rise to pressure differences and hence a forcing of the wind.
Since the Earth's axis of rotation is tilted about 23 degrees with respect to its orbit around the Sun, there is an imbalance of incoming solar radiance. Heating of the atmosphere therefore depends both on latitude and the Earth's position relative to the Sun. In general, the equatorial region receives more solar radiance than polar areas. This also explains why our Earth has seasons.

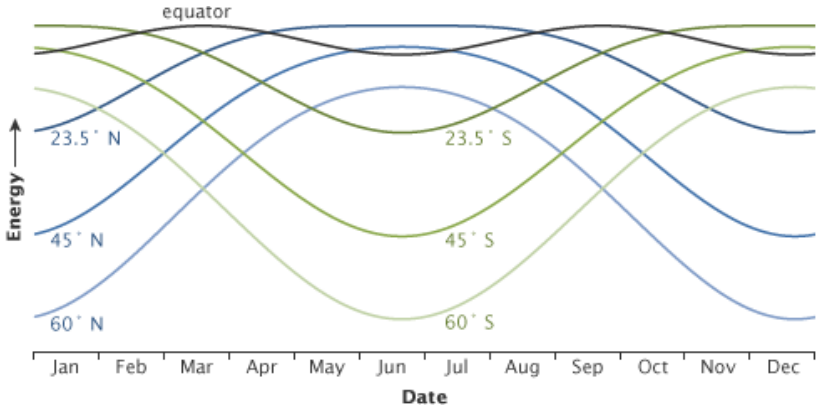

Figure 2.2: How the peak energy received at different latitudes changes throughout the year (Lindsey, 2009).

Figure 2.2 shows us the solar peak energy received at local noon each day throughout the year at different latitudes (Lindsey, 2009). Naturally, thermal heating based on solar radiance only occurs during daytime, and can therefore not be described mathematically by a single sinusoid (see Figure 2.3). For this, we must make use of a Fourier series. It is the components of this Fourier series that can be observed as tidal waves in the atmosphere.

$$J_\lambda(t) = \sum_n A_n(z,\theta,\lambda) cos\left(\frac{n2\pi t}{24} + \phi_n(z,\theta)\right) \tag{2.9}$$

Here $A_n(z,\theta,\lambda)$ are the amplitudes of the wave components given by the different values of n. As we give n values, tidal waves can be extracted from the formula. $(n = 1)$ is named the diurnal, $(n = 2)$the semidiurnal, $(n = 3)$ the terdiurnal. Although higher order components of the tidal wave may exist, Hibbins et al. (2007) have shown using a five-year dataset that the terdiurnal is the highest harmonic with a significant signal. Figure 2.3 shows us the heating of the atmosphere (red line), and the three first Fourier components (black) of the winds that this heating produces.

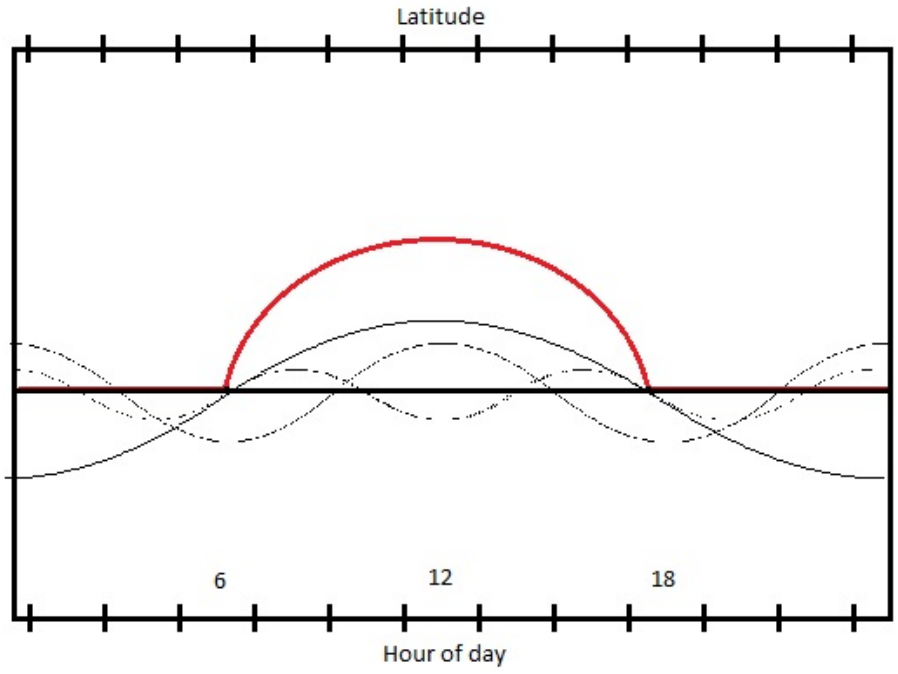

Figure 2.3: Illustration of the different Fourier components of the wind (black) that are produced by atmospheric heating (red) (Ekern, 2013).

Tidal waves can be categorised by migrating or non-migrating waves. Migrating waves follows Earth's rotation with the Sun. Non-migrating waves are forced at a single location and triggered when the Sun moves by. In the mesosphere the migrating tidal waves are the dominant ones (Salby, 1996).

2.3.2 Atmospheric Gravity waves

To describe gravity waves, we can think of water waves as an analogy. It is easy to understand the basic nature of water waves, since there are only two different mediums with two different densities: water and air. Water in a wave crest will be denser than the surrounding air, and tend to fall (due to gravity), while air in a wave trough is lighter than the surrounding water and will experience a buoyant force.

Although air is transparent, we know by the ideal gas law (eq. 2.5) that its density depends on pressure and temperature. In general it will decrease with altitude. This provides the possibility for parcels of dense air to rise above less dense air. If they are heavier than the surroundings, they can be dragged back down due to gravity. Since gravity is the restoring force, they are generally called gravity waves. These waves should not be confused with gravitational waves, a general relativistic phenomenon predicted by Albert Einstein in 1916.

As mentioned in section 2.2, for an air parcel to find itself heavier than its surroundings, a stable atmosphere ($\Gamma_a > \Gamma$) is required. Figure 2.4 illustrates this.

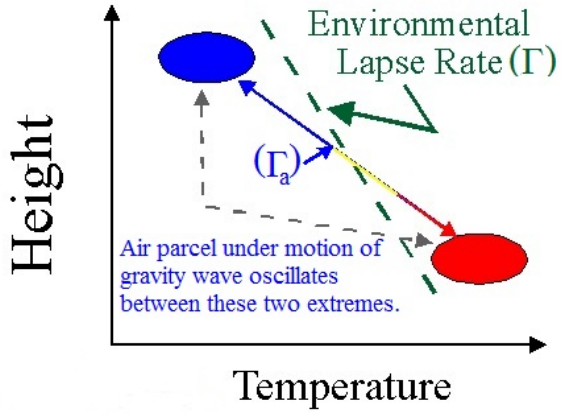

Figure 2.4: A parcel of air moved adiabatically in a stable atmosphere (Hocking, 2001).

There are several ways to generate these waves. The most obvious source in our case is wind flow over the Scandinavian mountain range. Other sources can be frontal and/or shear waves induced in the lower atmosphere. A frontal wave system can represent a mountain range in the sense that it will provide as a corrugated surface that oncoming airflow interacts with. Shear waves can create highly variable eddies that can launch freely propagating gravity waves further up in the atmosphere.

Figure 2.5 and 2.6 are two illustrations of how wind flow over a corrugated area generates gravity waves. In the more simple illustration (fig. 2.5) we see how the wave propagates upward in the atmosphere with its group velocity V_g, and its phase velocity, perpendicular to the group velocity, angled downward for upward energy propagation. It is also clear that for these orographic sources the horizontal phase speed is opposite in direction to

the wind speed.

This is also shown in figure 2.6, but here, more information are illustrated. We see that air is accelerated upwards and to the right on the windward side mountain (marked A), effectively compressing the air above and creating a higher pressure along this slope.
As discussed earlier, parcels of air that are moved adiabatically upwards will reach a point where it is cooler and denser than its surroundings and therefore fall back down due to gravity. As time goes by we can see this happen in figure 2.6. The blue lines represent the parcel being on its densest, this is followed by a low pressure region (L) and a downwards motion of the parcel until it finds itself hotter and lighter (red line) than its surroundings. From here the process repeats itself, effectively creating vertical columns of air oscillating.

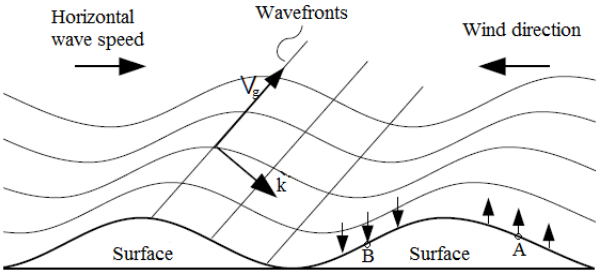

Figure 2.5: Generation of gravity waves due to wind flow over a corrugated surface. (Hennum, 2013)

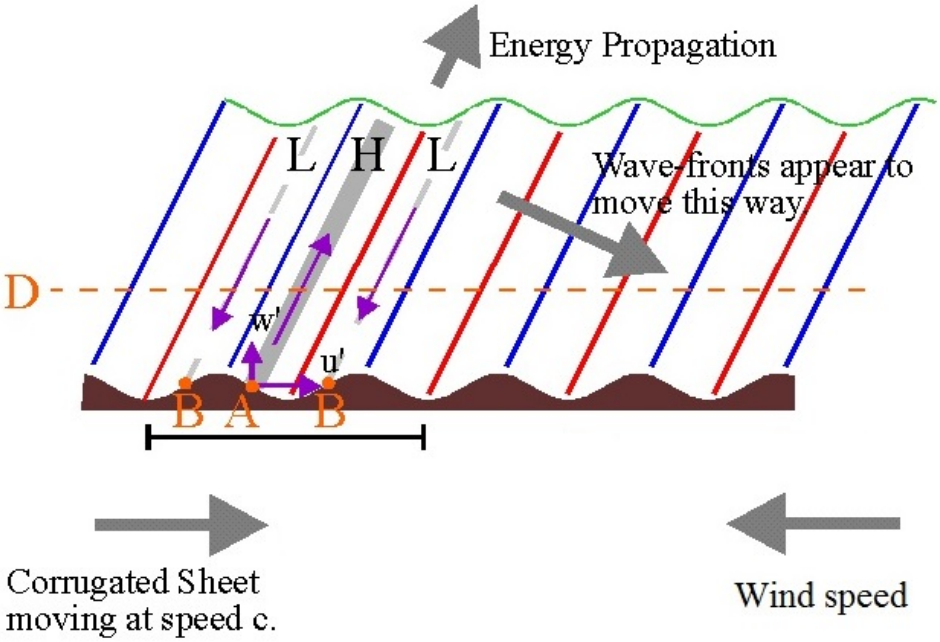

Figure 2.6: Detailed illustration of gravity wave oscillations (Hocking, 2001).

In effect, our corrugated surface could be the Scandinavian mountain range. Figure 2.7 shows us the mountain range (in red), and how it orientates itself in respect to our two measuring stations at Trondheim and Andenes. The marked distances in the figure are only rough approximations, based on information from Google Earth.

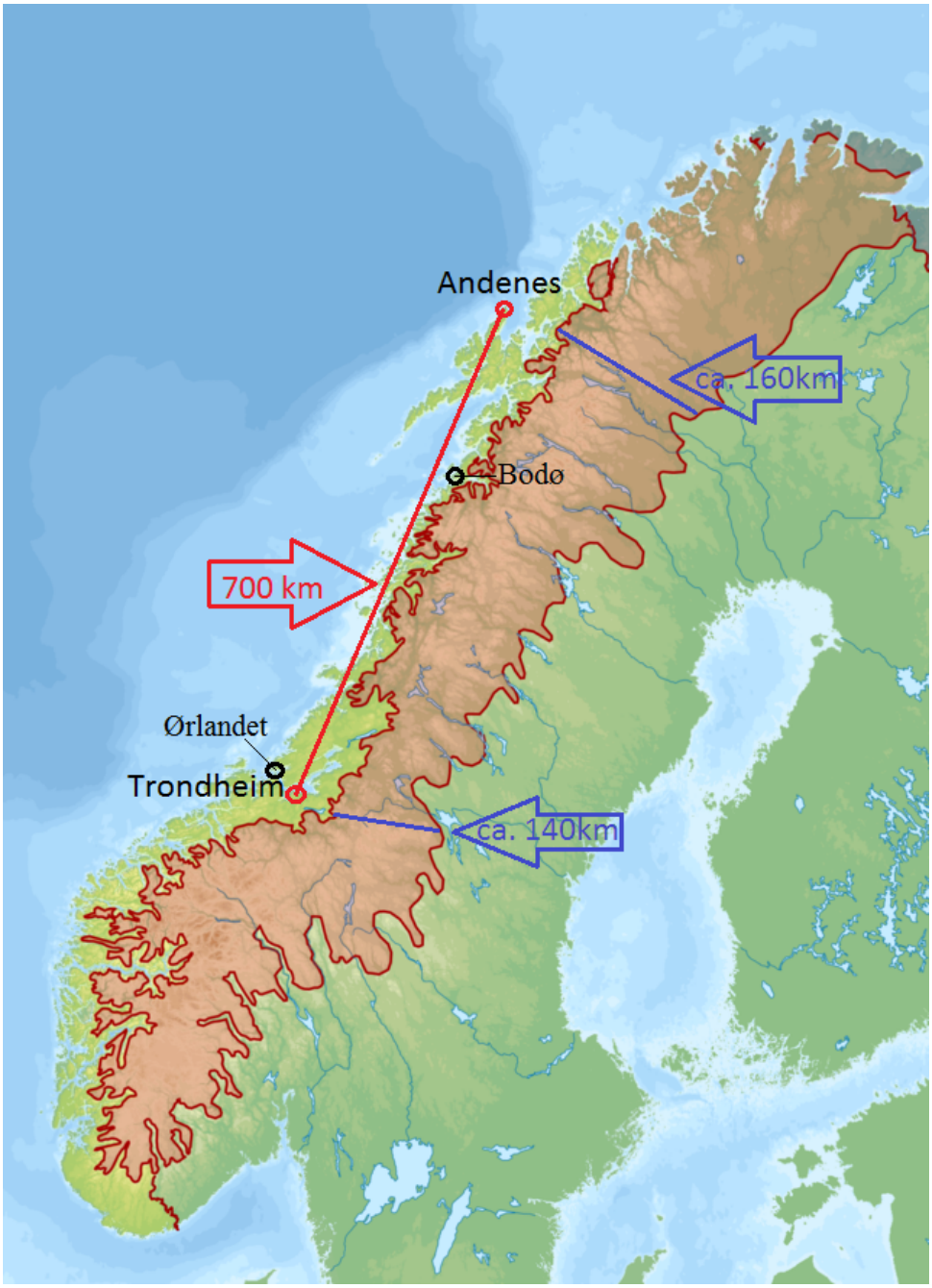

Figure 2.7: Scandinavian Mountains biogeographical region as defined by the European Agency of Environment and corrected by the Norwegian directorate for Nature Management. Red = Alpine region. Red circles indicate the locations of the SKiYMET radars, black circles indicate the locations of the balloon soundings.

When working with large-scale systems i.e wind flows over mesoscale mountains, one cannot ignore the rotation of the Earth. Meaning we are no longer in a inertial frame of reference. To predict and calculate movements at this scale, transformations of Newton's laws are necessary. As a result, the Coriolis force appears. This force causes moving objects to deflect clockwise in the Northern Hemisphere (and anti-clockwise in the Southern Hemisphere). Effectively this means that winds will not flow in a straight line from high pressure areas to low pressure areas, but northward (southward) motion will deflect towards the east (west) of these in the Northern (Southern) Hemisphere.

A way to describe how strongly a system is affected by the Coriolis force, is to calculate its Rossby number (R_o). For flow over mountains, the Rossby number may be defined as:

$$R_o \equiv \frac{U}{fL} \tag{2.10}$$

where U is the basic flow speed of the system, L is the horizontal scale of the orography, and $f = 2\Omega sin\phi$ is the Coriolis parameter (Ω is the rotation rate of Earth, and ϕ is the location's latitude).

If $R_o \gg 1$, the Coriolis effect on the system is negligible. If $R_o \ll 1$, the system is strongly affected by the Coriolis force, and the geostrophic approximation is usually valid. For $R_o \approx 1$, (as the case will be in general for flow over mesoscale mountains) the Coriolis effect large enough to play a role, but too small to be approximated by geostrophic theory (Lin, 2007)

In our case, the Rossby numbers for Trondheim $(63°N, 10°E)$ and Andenes $(69°N, 16°E)$ are respectively: $R_{o_{Trond}} \simeq 0.80$ and $R_{o_{And}} \simeq 0.67$, when setting $U = 10m/s$.
Thus, the Coriolis effect may introduce some deflection in any large scale wave motions, with the effect stronger at Andenes than at Trondheim.

2.4 Airglow

2.4.1 Chemistry of Hydroxyl

Hydroxyl (OH) nightglow is a weak emission of radiation originating in the upper mesosphere (a layer with a mean altitude of 87 ± 3 km, and a half-width of 5-8 km (Berge, 2011)), first observed by A. B. Meinel in 1948. The emission from the Meinel bands is mainly located in the infra-red (IR) region of our electromagnetic spectrum, and will be discussed in more detail in section 2.4.2.

Wayne (1985) gives us the relevant equations for production of OH in the mesosphere:

$$H + O_3 \rightarrow O_2 + OH^* \tag{2.11}$$

The hydrogen is regenerated via:

$$O + OH \rightarrow O_2 + H \tag{2.12}$$

The production rate of hydroxyl is dependent on both hydrogen and ozone, and is given by the equation:

$$P = k_{H+O_3}[H][O_3] \tag{2.13}$$

We note that the production of OH depends on the distribution of both H and O_3. Since the atmosphere will have an abundance of O_3 right after sunset, the production rate and intensity of OH often peaks at the beginning of the night (Hennum, 2013).

At night, reaction 2.3 reverses so that the main source of the ozone is the recombination of atomic and molecular oxygen. In addition, without sunlight, reaction 2.11 is the main loss process for the ozone. Thus, in steady state the ozone density is given by:

$$[O_3] = \frac{k_{O+O_2+M}[O][O_2][M]}{k_{H+O_3}[H]} \tag{2.14}$$

Where M is any third body (mainly N2). Substituting this into equation 2.13, we find that in steady state, the production of the vibrationally excited hydroxyl (OH^*) is:

$$P_{OH^*} = k_{O+O_2}[O][O_2][M] \tag{2.15}$$

Since the change of $[O]$ and $[O_2]$ with altitude is in the opposite direction below 95 km, wave motions will change the relative O to O_2 ratio at a given altitude. These changes will change the production of OH^* and the subsequent brightness of the nightglow. In addition, the moderate temperature dependence of reaction 2.15, proportional to $T^{-2.6}$, means that temperature changes induced by the adiabatic expansion and compression associated with the wave motions will moderate, somewhat, the wave amplitude of the OH emission.

2.4.2 The Meinel bands

Aden B. Meinel observed the hydroxyl airglow spectra for his thesis at UC Berkeley. He resolved and identified different airglow bands, which are now known as the Meinel bands. The radiation from the Meinel bands is due to a vibrational-rotational transition between different energy levels of OH^*. Reaction 2.11 produces exited hydroxyl from the vibrational state $v = 6$ to $v = 9$. As the lower vibrational levels are more stable, the molecule will radiate energy for each transition between vibration states.
Figure 2.8 shows the Meinel (3-1) and Meinel (4-2) bands. This means spectrum based on the transition between vibrational state $v = 3$ to $v = 1$, and $v = 4$ to $v = 2$ respectively.

For each band there are branches. These branches are determined by molecules change of rotational quantum number (ΔJ). Since ΔJ only takes the value of 0, 1 or -1, the band is split into three main branches: Q, R and P. Transitions where $\Delta J = 0$ are shown under the Q-branch, transitions where $\Delta J = 1$ are shown under the R-branch, and transitions where $\Delta J = -1$ are shown under the P-branch.
In this study, the intensity perturbations of the Meinel (3-1) P-branch will be used as an indicator of the existence of gravity waves in the mesosphere.

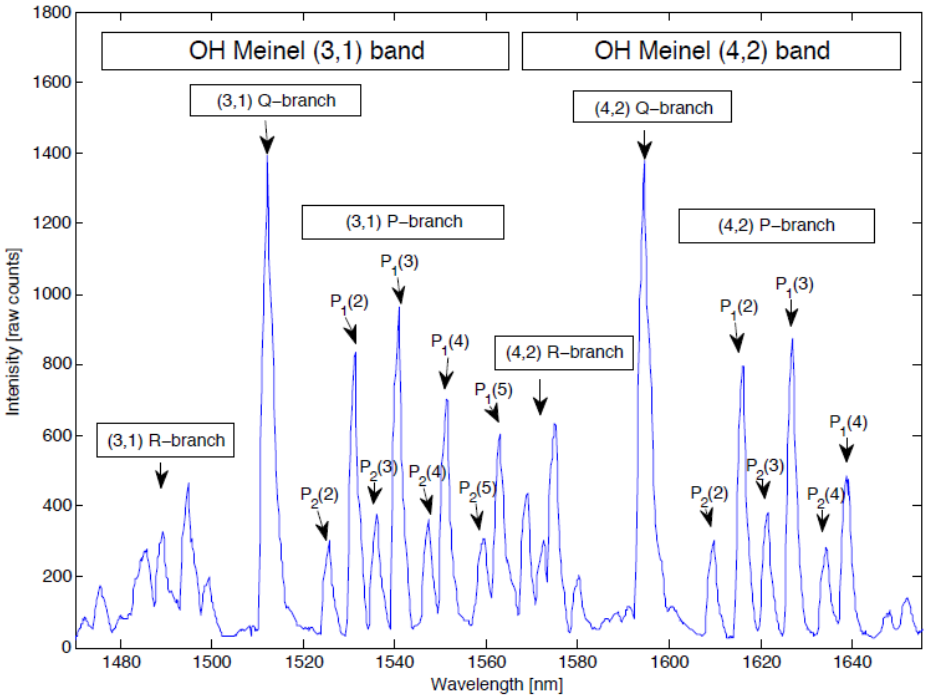

Figure 2.8: Meinel (3,1) and (4,2) bands nightly average spectrum between 29-30 November 2012, measured by Hennum (2013).

2.4.3 OH airglow perturbations induced by gravity waves

It is possible to detect and analyse gravity waves that propagate through airglow layers. Liu and Swenson, 2002 used a one-dimensional model to examine the relation between atmospheric gravity waves and airglow perturbations in the OH and O_2 layers.

By measuring airglow perturbations simultaneously in these layers, one can derive information regarding the vertical wavelength (λ_z), propagation direction and damping rate for the gravity wave. For simplicity, a damping factor of $\beta = 1$ where chosen. This represents saturated waves whose amplitude remains constant with altitude.

As mentioned earlier we only use data of airglow from the OH layer, so deriving λ_z will not be done. However, the energy propagation direction of the gravity wave will be determined in this study. Via their model, Liu and Swenson, 2002 derived an interesting graph showing the cancellation factor for gravity waves when moving through layers of airglow.

That is, for short vertical wavelengths, where many cycles of the wave exist within the airglow layer, the net perturbation is zero. On the other hand, the intensity amplitude of long vertical wavelength waves exceeds the density enhancement the wave due to the moderate temperature dependence of the rate coefficient and the increasing proportion of O with altitude mentioned in the previous section.

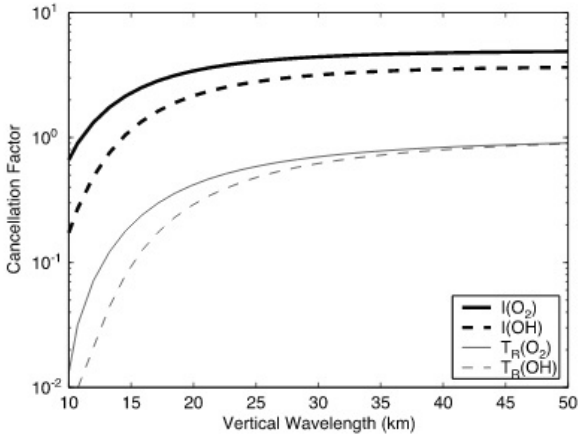

Figure 2.9: Cancellation factors of I' (thick lines) and T'_R (thin lines) for O_2 (solid lines) and OH (dashed lines), for waves with a period of 2 hr and the amplitude being constant with height ($\beta = 1$). (Liu and Swenson, 2002)

Figure 2.9 indicates that we need vertical wavelengths on the order of the thickness here approximately 10 km, to create significant perturbations of intensity and temperature in airglow-layers.

Chapter 3

Wind measurements

3.1 SKiYMET

Both at Trondheim ($63°N$, $10°E$) and Andenes ($69°N$, $16°E$) an All-Sky Interferometric Meteor Radar (SKiYMET) is used for observing meteors as they enter Earth's atmosphere. As these meteors hits the mesosphere they vaporize due to frictional forces (meteors with different masses evaporate at different heights), leaving behind a trail of ionized particles. These particles are carried by the surrounding, existing, wind system at their specific altitudes. Thus their motions effectively map winds in the mesosphere before they recombine after about four seconds.

To detect these winds, the transmitting antenna of the SKiYMET system sends a short electromagnetic pulse in form of a very-high frequency (34.21 MHz at Trondheim and 32.55 MHz at Andenes) radio wave into the mesosphere. These pulses will interact with perpendicular moving ionized particles. Backscatter is detected by five receiving antennas which are oriented to each other as a cross (fig 3.1). By using this setup, phase differences between the antennae of the meteor echoes are used to determine the position of the meteor. By observing how these phase differences of the moving trails change over time, the line of sight wind of the trail can be determined. Over the course of a day, approximately 10000 line of sight winds are collected between 70 and 110 km.
Using the collection line of sight winds from meteors in a 2 km wide altitude bin that have occurred over the course of an hour, a best fit zonal and meridional wind in that altitude bin can be determined. (Genesis Software).

Figure 3.1 shows a schematic view of a meteor radar system. There is a slight difference between the Trondheim and Andenes systems in that at Trondheim eight transmitters are used to direct more of the power towards zenith. Thus, while both systems detect 10000 meteors a day, most of these are between 15° and 50° off zenith at Trondheim, while most meteor detections at Andenes occur between 10° and 70° off zenith.

The data from the SKiYMET used in this study are called Hourly Wind Data (hwd),

and can be wieved in matlab as a structure containing information about the zonal (u) and meridional (v) winds each hour at the altitudes of 82km, 85km, 88km, 91km, 94km and 98km. The number of meteors detected (pts) each hour for these altitudes are also available in the hwd-file and can be used as an indicator of the quality of the wind measurement. Generally, the hourly wind observations over the 82-98km altitude range used in this study have an accuracy of 2 m/s (R. de Wit, personal communication via P. Espy).

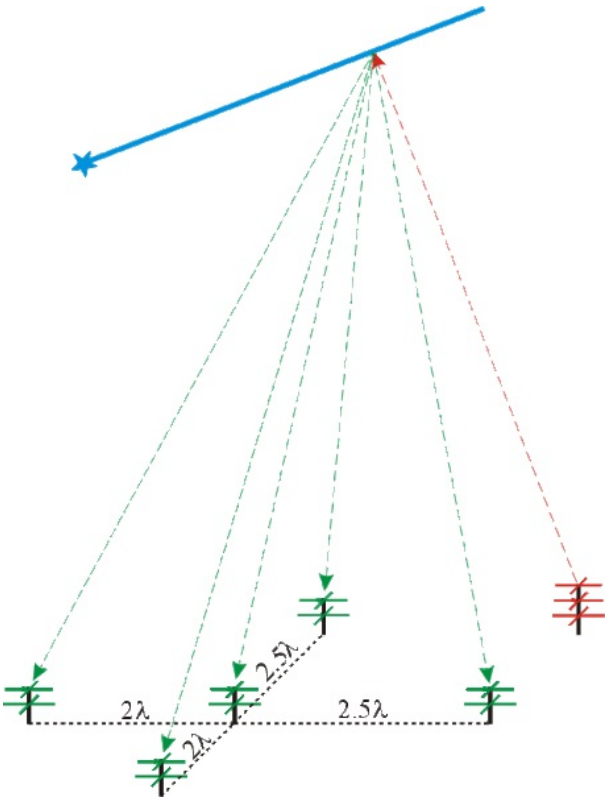

Figure 3.1: Scheme of meteor observations with radars consisting of 1 transmitting antenna (red) and 5 receiving antennas (green) (Leibniz-Institut für atmosphären physik).

3.2 Balloon soundings

Sounding balloons are a tool used by meteorologists for a variety of causes, but mainly to provide information about current temperature, humidity and wind speeds in the troposphere and lower stratosphere. Routinely based launches happens twice a day, at 00:00 UTC and 12:00 UTC. For us, the balloon soundings provides measured wind speeds and directions over the mountain range and up to 25 km (lower stratosphere). Data from measuring stations at Ørlandet (63.70°N, 9.60°E) and Bodø (67.25°N, 14.40°E) are used to provide data for this study.

Chapter 4

Airglow Spectrometer

For the spectroscopy of the hydroxyl nightglow, an Andor Shamrock SR-163 spectrograph is used. The spectrograph is based on a Czerny-Turner layout (fig. 4.1), and has a focal length of 163 mm and an f-number of f/3.6.

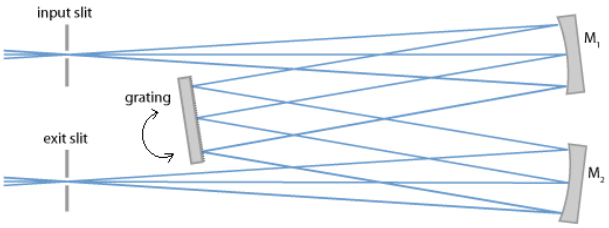

Figure 4.1: Simplified design of a Czerny-Turner layout.

The principle behind a Czerny-Turner design is shown above. The first concave mirror (M_1) has its focal point at the entrance slit, which collimates the light incident on the reflective grating. The diffracted light is incident on a second concave mirror (M_2), which then forms an image of the entrance slit at the exit focal plane. Since each wavelength dispersed from the grating will have a different incident angle on this second mirror, their images will be dispersed across the exit focal plane. The grating may be rotated to select which wavelengths are incident upon the camera detector. The grating used in the Shamrock SR-163 is blazed for a wavelength of 1600 nm, has 600 lines/mm and a nominal dispersion of 7.11 nm/mm.

The camera attached to the exit slit is the Andor iDus InGaAs μ1.7 DU491A. It is a linear photo diode array (PDA) detector with 1024 pixels. The operating wavelength range is given to be 600-1700 nm and it has a minimum exposure time of $1.4\mu s$. The camera also has a built in cooling system, to reduce thermal noise induced by dark current. The sensor can be cooled down to -90° depending on the temperature of the surroundings. While it may seem that one should run the detector as cold as possible, an adverse effect of the cooling is to reduce the long-wavelength response of the detector due to reduced electron mobility in the diode. In order to achieve low dark current while preserving the long wavelength response, the detector was cooled to -55°, where the small

change in dark current with temperature ensures stable operation.

Figure 4.2 shows the thermal noise measured with 1 second integration time for different temperatures. Figure 4.3 shows the Andor Shamrock SR-163 spectrograph (left) and the iDus InGaAs μ1.7 camera (right). Figure 4.4 is a picture of the spectrometer installation at Dragvoll, Trondheim.

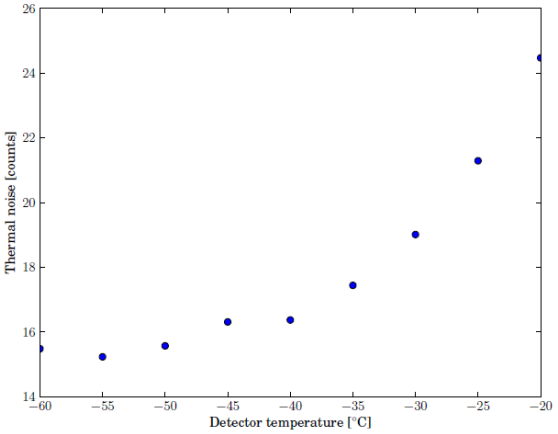

Figure 4.2: Thermal noise of the detector at different detector temperatures, measured with 1 second integration time (Hennum, 2013).

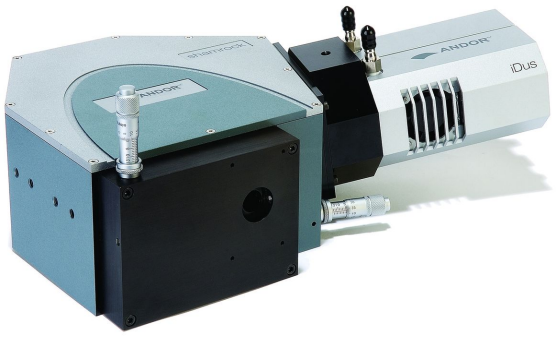

Figure 4.3: The Shamrock SR-163 with the iDus InGaAs camera attached to the right.

Figure 4.4: The spectrometer installation as seen from above.

Chapter 5

Method

5.1 Curve fitting to remove tidals

In order to detect any anomalies i.e. our gravity wave in the atmosphere, we need to remove the dominant tidal waves in the dataset. This is done by using a curve-fitting application ("cftool") in Matlab.

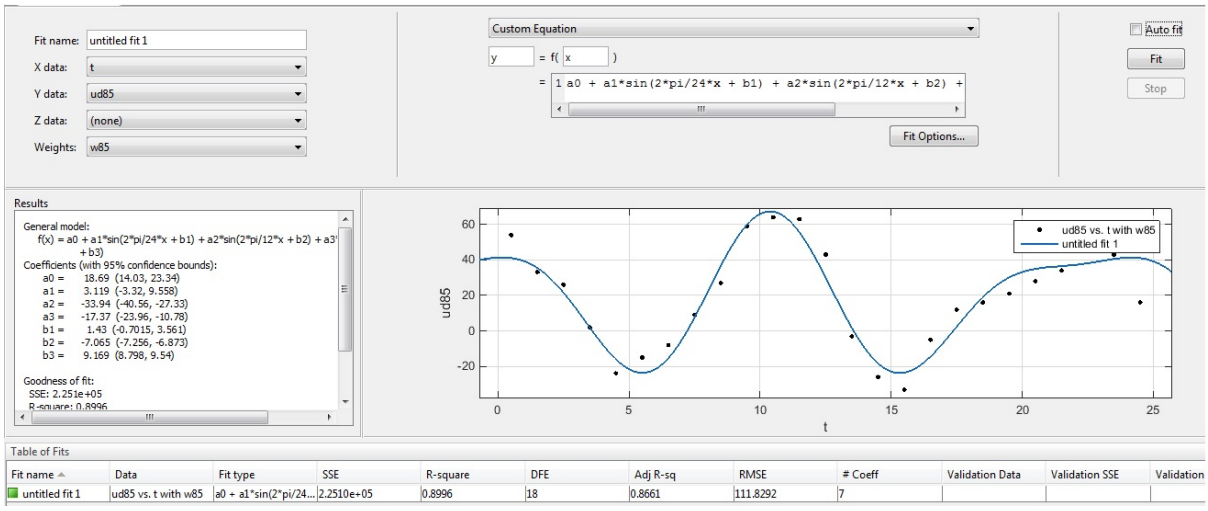

Figure 5.1: Curve fitting app in matlab.

Figure 5.1 demonstrates how components of tidal waves can be found in raw data from SKiYMET. By inputting a time vector and corresponding raw data from the hwd-files, a graph is shown, representing the raw data points as black dots.
By typing in a custom equation containing an offset and sinus waves with periods equal to the diurnal, semidiurnal and terdiurnal, cftool will approximate the corresponding amplitudes and phases and return a fit (blue line) which contains our tidal waves in the dataset. Since the numbers of meteors per hour are not constant, the data are weighted by the number of meteors used in the wind determination for the fitting (given as .pts in

the hwd-file).

To get the hourly anomaly winds, values representing the tides resulting from our fitted equation are subtracted from the raw data for each time interval. This is done for both the zonal (u) - and the meridional (v) velocities, at the height of 85km, 88km and 91km. In this way mean anomaly components u' and v' are found by averaging these three layers.

5.2 FFT Analysis

To find remaining frequencies of the different wave components in the dataset, the Fast Fourier Transform (FFT) where used. In principle, this algorithm tries to find the best set of sine waves that will reproduce the dataset.

To reproduce the cut-off for a finite set of data, the FFT produces many high-frequency components. In order to reduce this effect, a Hamming-window is applied. Each side-lobe related to the frequency peaks of the spectrum are considerably damped. However the frequency peaks will get wider, and thus the corresponding errors in localizing the frequency of the oscillation slightly larger (Press et al., 1992).

When working with a low amount of datapoints (N), it is beneficial to add zeros to the dataset (zero-padding). Our datasets will contain 96 and 25 values for a five-night and a 24 hour period, respectively. The FFT calculates $\frac{N}{2}$ frequencies between 0 and the Nyquist-frequency ($\frac{1}{2F_s}$). By increasing N with zero-padding, we effectively increase the number of frequencies calculated, smoothing out the resulting FFT plot.

When referring to detected frequencies, the Full-Width at Half-Maximum (FWHM (Δf)) is used in order to provide information regarding its uncertainties. The FWHM is a measure best used on Gaussian formed curves, where it will provide a 76.2% chance of the true value existing within its interval. For amplitude spectres where the FWHM cannot be read out of the graph, a Gaussian approximation will be added, to provide this possibility.

5.3 Cross-correlation

The cross-correlation function is a measure for the relationships of values from two different sets of data at two times separated by a timestep τ. In matlab, the function "crosscorr" is used. This function plots the correlation between two time series with 95% confidence bounds, informing us of the significance of the correlation. Also, the timestep or lag at which the cross-correlation maximizes gives us the phase difference between the datasets (Girod et al., 2001).

5.4 Hodographs

In a hodograph, meridional wind perturbations are plotted against the zonal wind perturbations at a specific time, from a start altitude to an end altitude.
By doing this, one can determine the direction of the wave's vertical energy propagation, and horizontal propagation relative to the background wind by evaluating a hodograph. For us, in the Northern Hemisphere, a clockwise rotation of the gravity-horizontal wave wind vector is associated with a wave having upward energy propagation and a downward phase velocity. The horizontal propagation direction of the wave lies along the major axis of the elliptical hodograph (Moffat-Griffin et al., 2011).

5.5 Lomb-Scargle Analysis

As opposed to the meteor wind data, the data given in the time domain by the Airglow Spectrometer are unevenly spaced and somewhat incomplete and requires interpolation to fill the gaps. This prohibits the use of the FFT to determine the periodic behaviour of the perturbations of OH temperature and intensity. In order to determine these cycles, another method is used, called the Lomb-Scargle Periodogram.
The Lomb-Scargle Periodogram estimates a frequency spectrum based on a least square fit of sinusoids (Glynn et al., 2006). Since this is a fitting technique, it does not require an even time sample as the FFT method does.

Chapter 6

Results

Chapter outline Matlab R2014a is used to complete the following analysis.
As mentioned, the SKiYMET radars calculates and stores hourly wind data (hwd) in hwd-files. When read into Matlab, the information is available in structures, making it easy to derive and analyse values of interests. This study focuses primarily on the night where Hennum (2013) detected gravity wave activity (the night between the 29-30th of November 2012). However, the analysis begins by considering hwd-data from a six day (or five-night) period with our night in the center. The dates 27th November - 02nd December are loaded into Matlab.

The chapter will mainly be divided into three parts. Analysis regarding data from Trondheim. Analysis regarding data from Andenes. And a section where the cross-correlation function is used between the results.

Since the dataset requires analysis for winds both in zonal and meridional direction, these three sections are divided into two subsections: one for zonal and one for meridional analysis. For each of these subsections we start out by analysing the five-night period, before we finish up by looking closer at our night of interest, 29-30th of November, 2012.

While this is an extensive amount of material to go through, the procedure for analysis is the same for each dataset. In order to prevent self-repetition in this chapter, a deeper description and explanation of the results will only be given for the Trondheim zonal wind analysis. For the remaining analyses, figures and results are presented, but not discussed in detail.

To conclude the sections related to Trondheim and Andenes data, a figure presenting the hydroxyl intensity perturbations of the (3-1) Meinel bands are given together with a Lomb-Scargle periodogram for the 24 hour period. This study focuses primarily on the data collected from the SKiYMET-radars to detect any gravity waves, but the hydroxyl perturbations may assist in showing sheared oscillations at the two measuring sites.

6.1 Trondheim data

6.1.1 The five-night period (zonal analysis)

Removing tidal components

In order to fit the tides while allowing for temporal variation of their amplitudes, the datasets are divided into blocks of 24 hour periods. Stretching from 11:30 a.m. one day to 11:30 a.m. the next day (fig. 5.1). The fitted curves are then added together, completing a five-night cycle, and subtracted from the raw data. By doing this we are left with the residual of the wind system, or "the anomaly wind". This is done for the altitudes of 85 km (fig.6.1), 88 km (fig.6.2) and 91 km (fig.6.3).

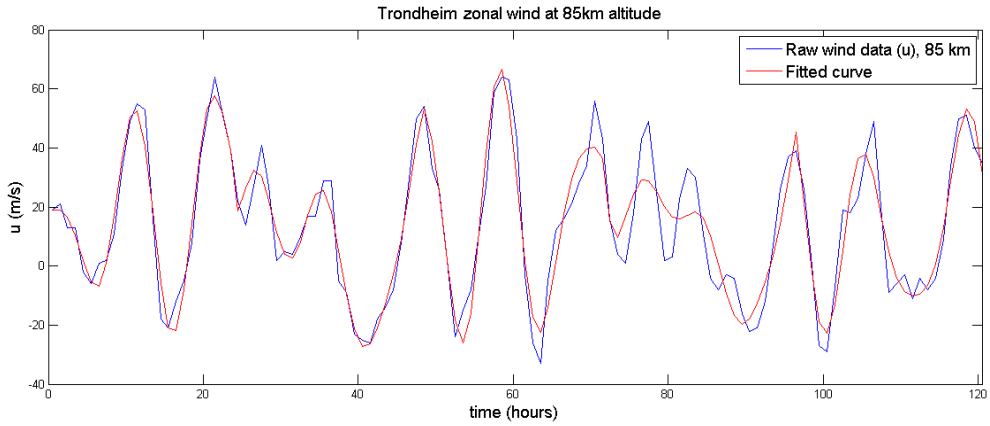

Figure 6.1: Raw zonal wind data from 85 km altitude (blue) plotted against its fitted curve (red).

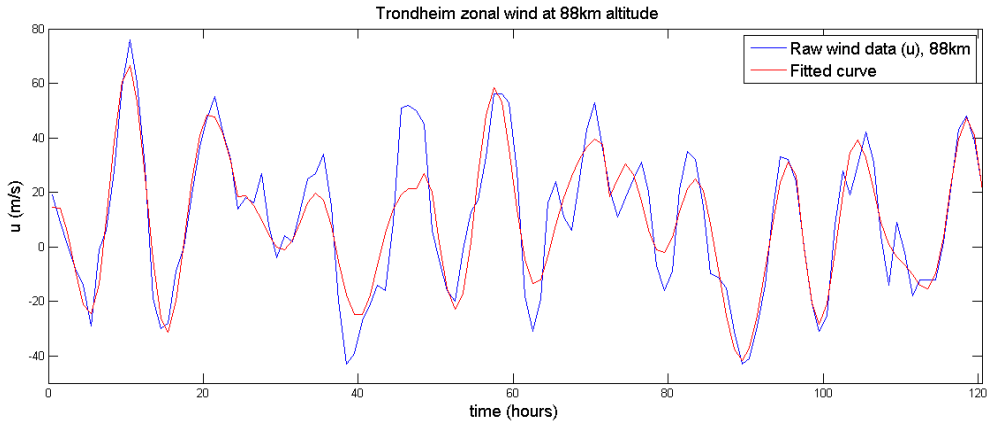

Figure 6.2: Raw zonal wind data from 88 km altitude (blue) plotted against its fitted curve (red).

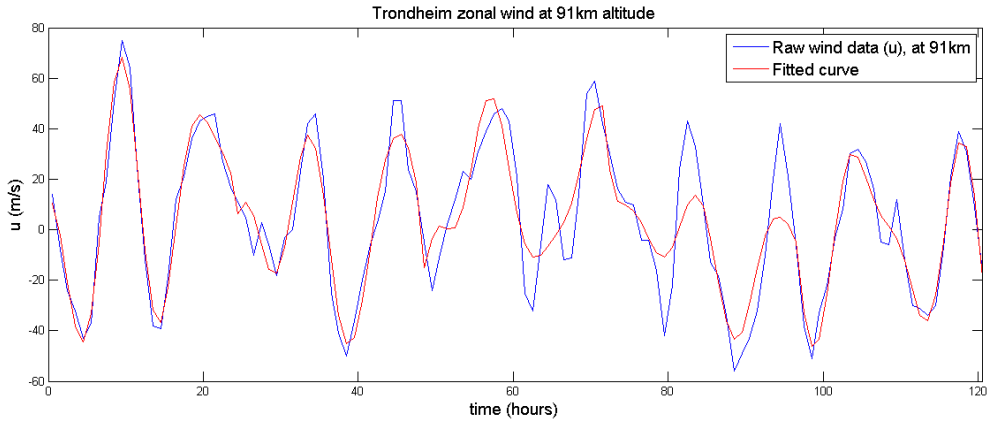

Figure 6.3: Raw zonal wind data from 91 km altitude (blue) plotted against its fitted curve (red).

To evaluate the goodness of the fit, Matlab's Curve fitting toolbox provides a few options. To start with, figure 6.1, 6.2 and 6.3 visualize the fitting of the raw wind data using only the diurnal, semidiurnal and terdiurnal as wind components. We can see that the tidal waves are dominant in the mesosphere.

The R-square (R^2) value is a numerical guideline for the goodness of the fit. This value is a measure of how successful the fit is in explaining the variation of the raw data. The closer this value is to 1, the better the fit. During the first night, the R^2 value at 85km is equal to 0.9535. Meaning that the fit explains 95,35% of the variation in the data about the average. The table below (table 6.1) shows all the R^2 values of the zonal five-night cycle in Trondheim.

		Dates				
		27-28th	28-29th	29-30th	30-01st	01-02nd
Altitudes	85km	0.9593	0.9369	0.9174	0.7113	0.8921
	88km	0.9532	0.7024	0.7793	0.8553	0.9068
	91km	0.9676	0.8980	0.7073	0.6945	0.9439

Table 6.1: Overview of R^2 values for the zonal winds over Trondheim

Generally our R^2 value are good. However, close to 1 values were never a goal, since we are not fitting a curve to explain the whole dataset. We are merely fitting a curve that can explain the tidal waves. A variation beyond this is expected, and noted around the dates 29-30th and 30-01st where the R^2 values seems to drop.

The toolbox also calculates 95% confidence bounds related to the fitted coefficients. The list below, shows the fitted coefficients with confidence bounds for the first night (27-28th of November) at altitude 85 km. (The coefficients relate to the fitted model's equation: $y = a0 + a1sin(\frac{2\pi x}{24} + b1) + a2sin(\frac{2\pi x}{12} + b2) + a3sin(\frac{2\pi x}{8} + b3) + a4sin(\frac{2\pi x}{48} + b4)$):

- a0 = -25.6 (-96.22, 45.01)
- a1 = 35.78 (-12.61, 84.17)
- a2 = 32.98 (24.86, 41.09)
- a3 = 12.48 (6.907, 18.05)
- a4 = 71.04 (-40.46, 182.5)
- b1 = 1.498 (1.234, 1.762)
- b2 = 2.197 (1.919, 2.476)
- b3 = 4.95 (4.522, 5.378)
- b4 = 12.47 (12.34, 12.61)

The biggest uncertainty lies within the amplitude coefficients of the diurnal component (a1), and the component of the two-day wave (a4). This is expected, since their periods (24 and 48 hour) span the whole dataset (24 hours).

Finally, the residual, which we take to be the anomaly wind can also say something about the goodness of the fit. Normally if the residual of a fit appears to behave randomly, we would say we have a good fit. Should there be coherent signals remaining, for example

quasi-periodic gravity waves, we would expect to see a non-random, periodic behaviour in the residuals.

The anomaly winds

The anomaly winds are given by subtracting the fitted model (red line in fig.6.1, 6.2 and 6.3) from the raw data (blue line in those figures). The resulting anomaly winds are given below:

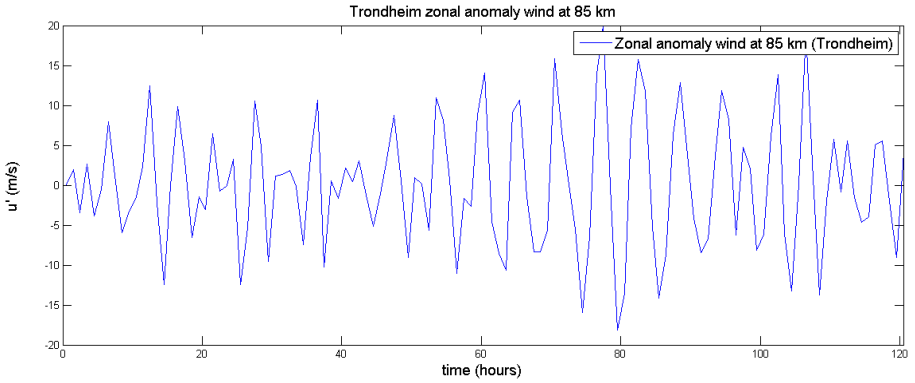

Figure 6.4: Zonal anomaly wind at 85 km (Trondheim).

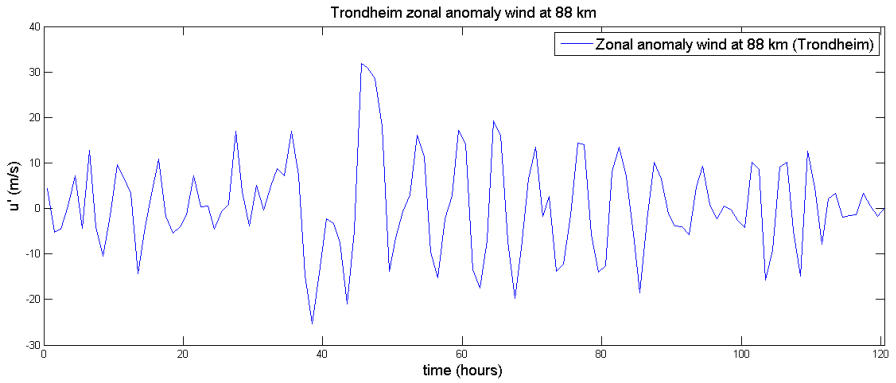

Figure 6.5: Zonal anomaly wind at 88 km (Trondheim).

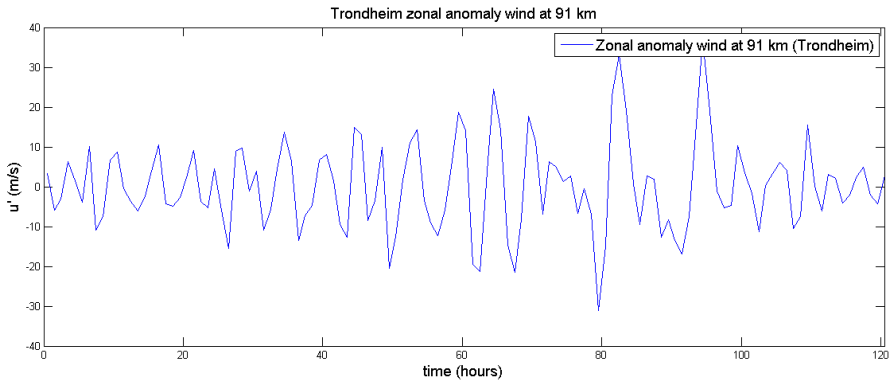

Figure 6.6: Zonal anomaly wind at 91 km (Trondheim).

From the above figures, it is clear that the residuals of the fits are of periodic nature. Indicating additional wind structures (beyond our tidal winds) in the Mesosphere.

Mean anomaly wind

After finding the anomaly winds for the different altitudes, the next step is to average these winds around 88 km in order to simulate those structures that would also be detectable in the 8 km thick hydroxyl airglow layer. The related errors are found as normalized standard deviations for each time point. The below figures (fig.6.7 and fig.6.8) shows us the mean zonal anomaly wind of Trondheim from the 27th of November to the 2nd of December 2012, with and without errorbars:

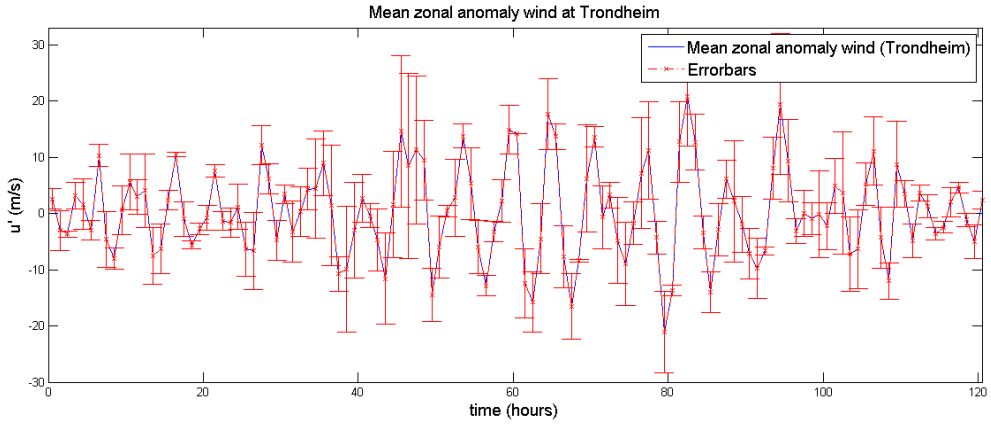

Figure 6.7: Mean zonal anomaly wind over Trondheim, with errorbars.

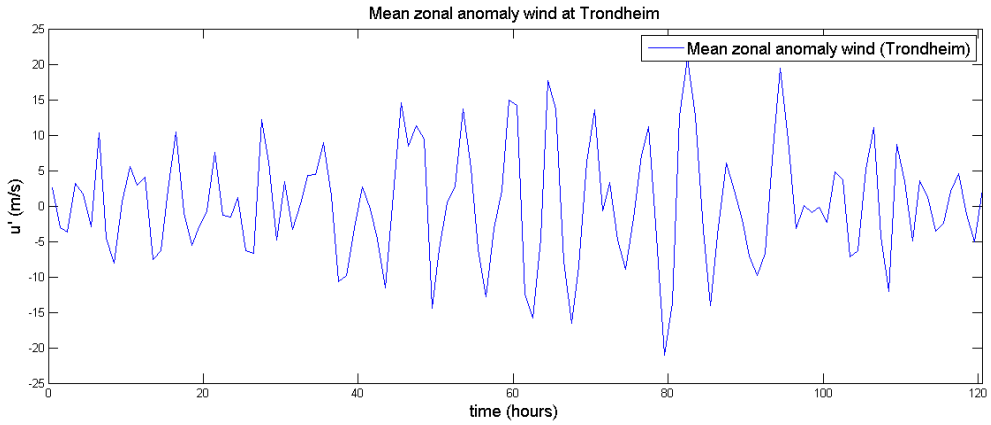

Figure 6.8: Mean zonal anomaly wind over Trondheim.

The Fast Fourier Transform

To analyse the data further, the system is transformed via the FFT to determine its periodic behaviour. Figure 6.9 shows a major peak at the frequency $0.17h^{-1}$, with a FWHM (Δf) of $0.022h^{-1}$. This peak represents a period of 6.0h (5.6h, 6.3h). Although tempting to attribute this to a higher order (4th) harmonic of the tide, we remember the study of Hibbins et al. (2007) which tells us that this is probably not the case.

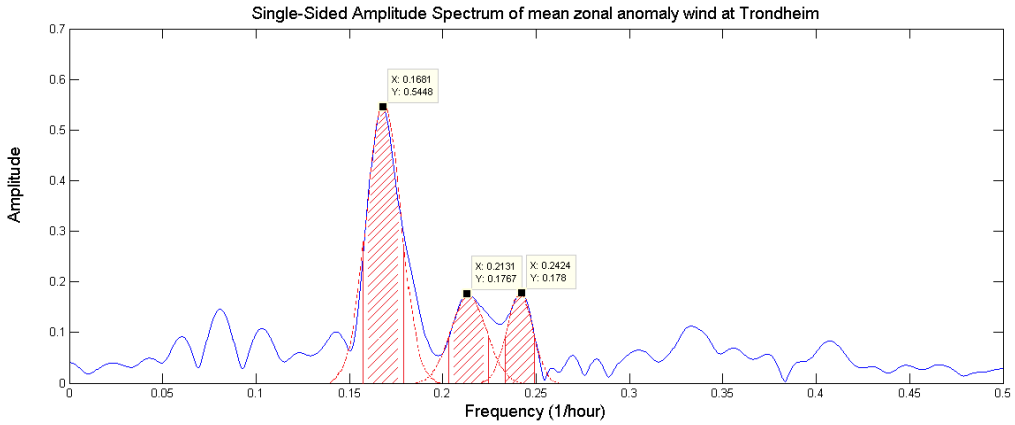

Figure 6.9: FFT of the mean zonal anomaly wind over Trondheim.

Two other peaks are interesting. The peaks located at frequencies of $0.21h^{-1}$ ($\Delta f = 0.020h^{-1}$) and $0.24h^{-1}$($\Delta f = 0.017h^{-1}$) give periods of 4,7h (4.5h, 4.9h) and 4,1h (4.0h, 4.3h) respectively. This concludes the analysis for the five-night period.

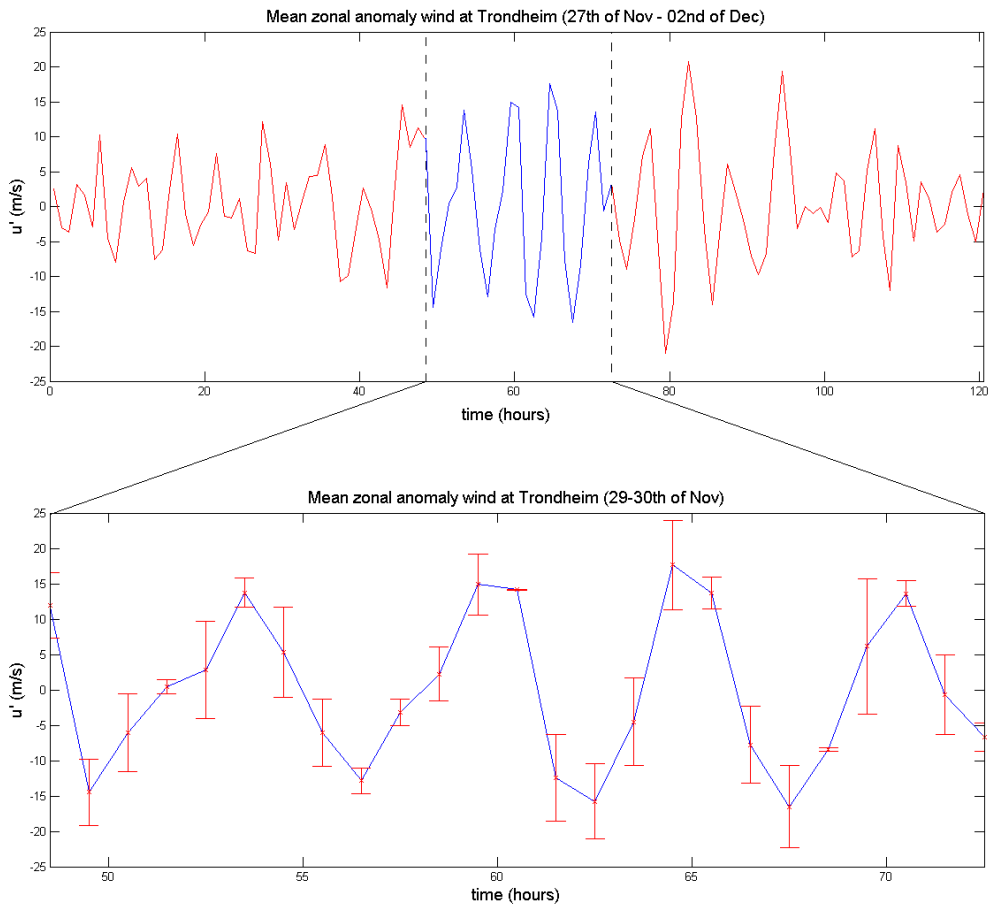

Figure 6.10: Transition from our five-night period to our night of interest, the 29-30th of November 2012, with errorbars.

6.1.2 The 24 hour period (zonal analysis)

Figure 6.10 reveals the datapoints for further analysis. The data in the lower plot concentrates about the mean zonal anomaly wind over Trondheim from 11:30 a.m. the 29th of November to 11:30 a.m. the 30th of November 2012.

The Fast Fourier Transform

Again, to find the periodic behaviour of our data, the FFT is used:

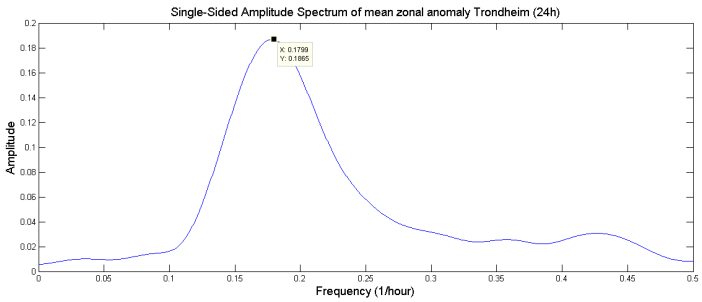

Figure 6.11: FFT of mean zonal anomaly wind during 29-30th of November over Trondheim.

A single peak at the frequency of $0.18h^{-1}$ with a FWHM (Δf) of $0.10h^{-1}$ gives a period of 5.6h (4.4h, 7.3h).

6.1.3 The five-night period (meridional analysis)

Removing tidal components

The following figures are important for the meridional analysis:

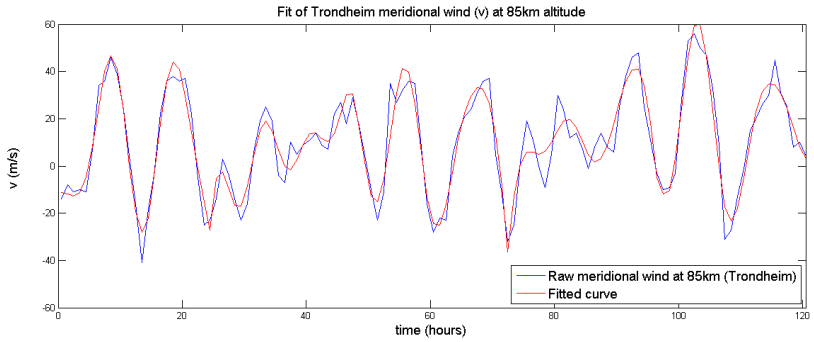

Figure 6.12: Raw zonal wind data from 85 km altitude (blue) plotted against its fitted curve (red).

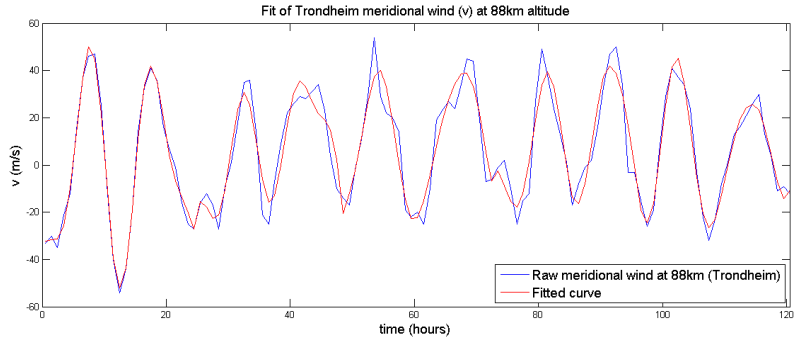

Figure 6.13: Raw zonal wind data from 88 km altitude (blue) plotted against its fitted curve (red).

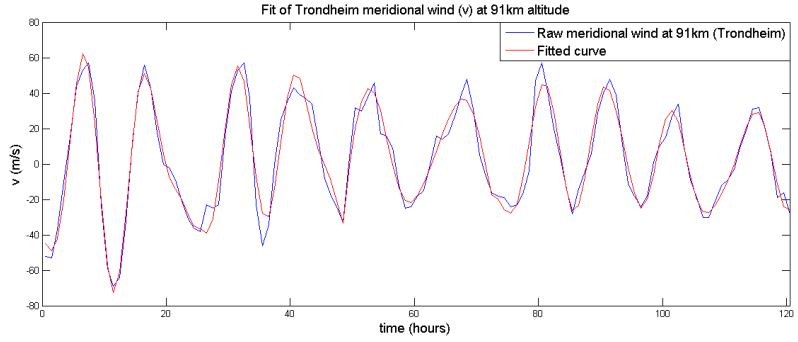

Figure 6.14: Raw zonal wind data from 91 km altitude (blue) plotted against its fitted curve (red).

Table of R^2 values:

		Dates				
		27-28th	28-29th	29-30th	30-01st	01-02nd
Altitudes	85km	0.9551	0.8257	0.9192	0.8197	0.9363
	88km	0.9926	0.8728	0.8788	0.8683	0.9688
	91km	0.9838	0.9120	0.9141	0.9286	0.9591

Table 6.2: Overview of R^2 values for the meriodal winds over Trondheim

Mean anomaly wind

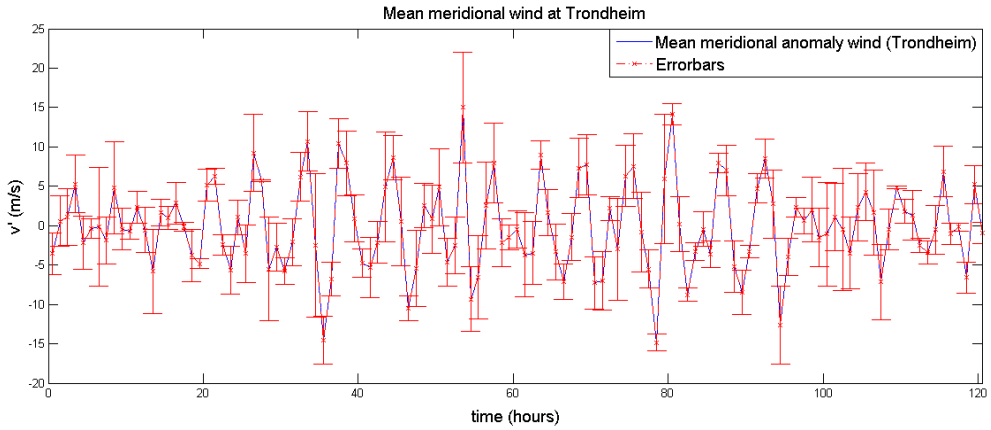

Figure 6.15: Mean meridional anomaly wind over Trondheim, with errorbars.

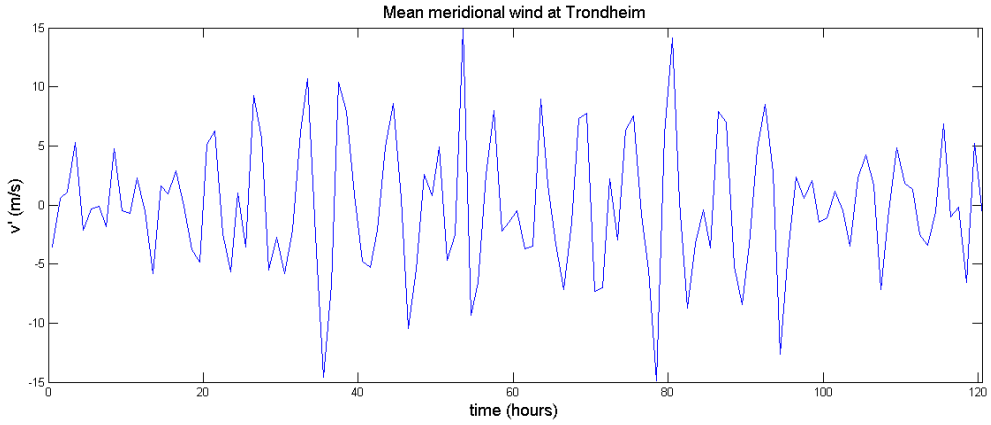

Figure 6.16: Mean meridional anomaly wind over Trondheim.

The Fast Fourier Transform

In figure 6.17, three peaks are highlighted. The first one at frequency $0.17h^{-1}$ with a period of 6.0h (5.7h, 6.3h). Then we got peaks of frequencies $0.19h^{-1}$ and $0.26h^{-1}$, giving periods of 5.3h (5.0h, 5.5h) and 3.9h (3.7h, 4.0h) respectively.

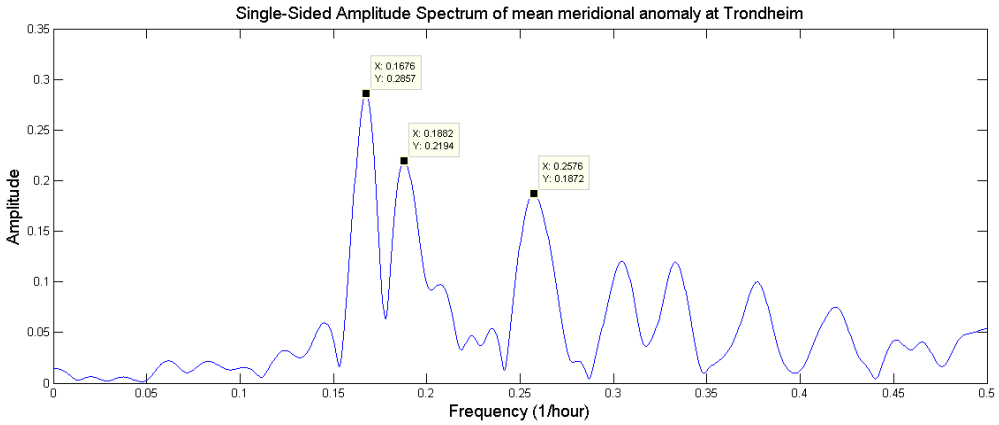

Figure 6.17: FFT of the mean meridional anomaly wind over Trondheim.

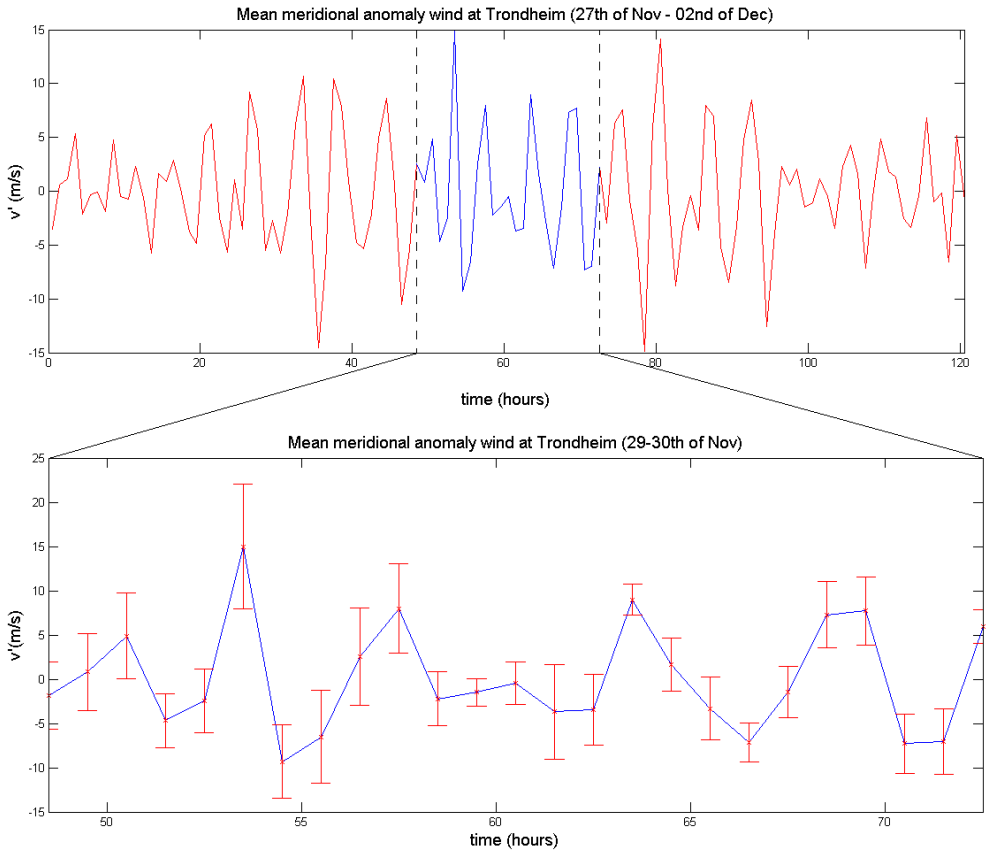

Figure 6.18: Transition from our five-night period to our night of interest, the 29-30th of November 2012, with errorbars.

6.1.4 The 24 hour period (meridional analysis)

The Fast Fourier Transform

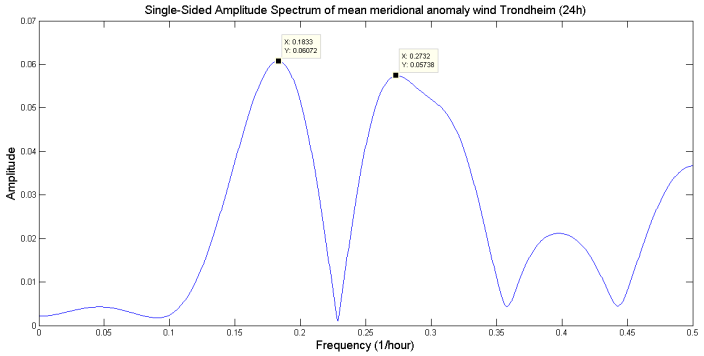

Figure 6.19: FFT of mean meridional anomaly wind during 29-30th of November over Trondheim.

For the 24 hour mean meridional anomaly wind (fig.6.33), two frequencies are present.

From the first peak, one can extract the data $f_1 = 0.18h^{-1}$ with $\Delta f_1 = 0.071$ that gives a period of 5.5h (4.7h, 7.0h). The second frequency ($f_2 = 0.27h^{-1}$ with $\Delta f_2 = 0.094h^{-1}$) gives a period of 3.7h (3.0h, 4.1h).

6.1.5 Energy propagation

Figure 6.20 shows a contour plot of a cross-correlation function between the zonal wind at 88 km and the zonal winds at the different altitudes to determine their phase relationship. Dark red colour indicates correlation, while dark blue colour indicates anti-correlation. Here, any positive (negative) lag tells us that the anomaly wind at that altitude lags (leads) the 88 km anomaly wind. The phase change between the altitudes are plotted in the right panel. The phase relations between the altitudes tell us that the lower altitudes lags the upper altitudes, giving us a downward phase propagation in time and an upward energy propagation in accordance to Hocking (2001).

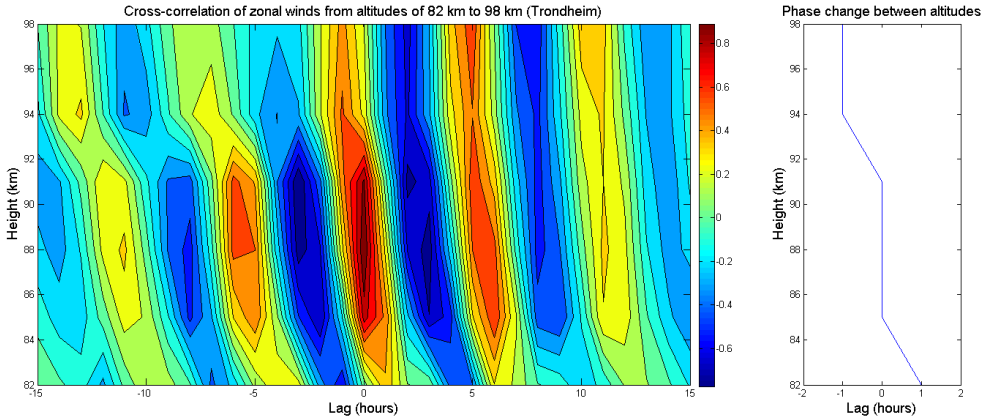

Figure 6.20: Left panel: Cross-correlation of zonal winds over Trondheim. All winds are correlated with the data extracted from the altitude of 88km. Red colour represents correlation and blue denotes anti-correlation. Right panel: vertical profile of phase change between zonal anomaly wind at 88 km altitude and zonal anomalies of different altitudes.

For figure 6.21 we see that the cross-correlation function wants both the lower and the higher altitudes to lead the 88 km meridional wind. Instead of this being true, one can argue that the lower altitude meridional wind actually lags with more than half a period (orange spot at a 5 hour lag in the 82 km altitude). Matlab will interpret this as a (less than a half period) lead, giving rise to this visual effect. Looking at the contour plot, this might make sense.

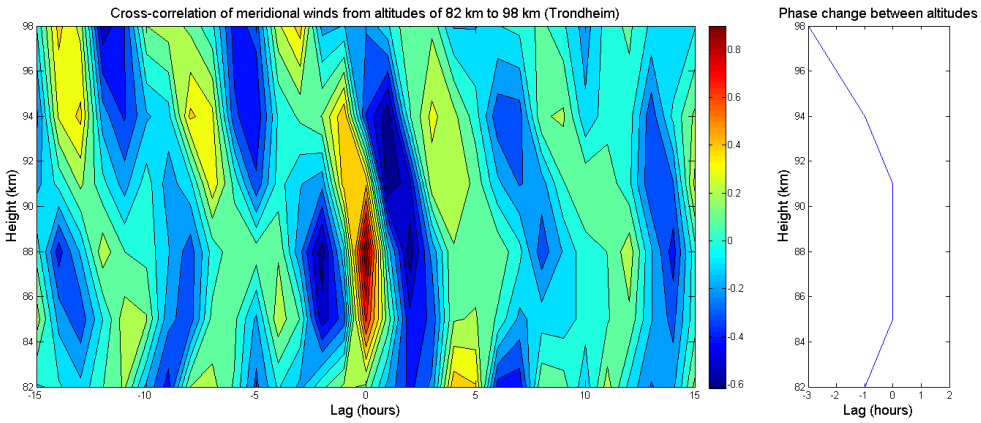

Figure 6.21: Left panel: Cross-correlation of meridional winds over Trondheim. All winds are correlated with the data extracted from the altitude of 88km. Red colour represents correlation and blue denotes anti-correlation. Right panel: vertical profile of phase change between meridional anomaly wind at 88 km altitude and meridional anomalies of different altitudes.

By plotting meridional and zonal anomaly wind perturbations against each other at different altitudes for a specific time, one gets a hodograph. As described in section 5.4, this gives us information of the energy propagation of a wave. Figure 6.22 is the hodograph for the Trondheim anomaly wind at 04:30 p.m. A clockwise rotation agrees with the upward energy propagation direction given by the cross-correlation between the anomaly winds at different altitudes (fig.6.20 and fig.6.21).

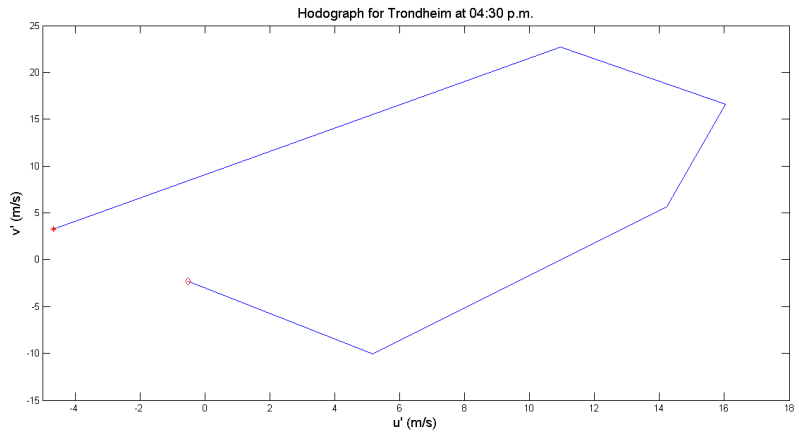

Figure 6.22: Trondheim meridional anomaly wind perturbation plotted against the zonal anomaly wind perturbation. The red asterisk indicates the lowest altitude measurements; the red diamond indicates the highest altitude measurements.

6.1.6 Perturbations of the Hydroxyl Intensities

The following figure shows the intensity perturbations of the (3-1) Meinel P-branch, measured in Trondheim.

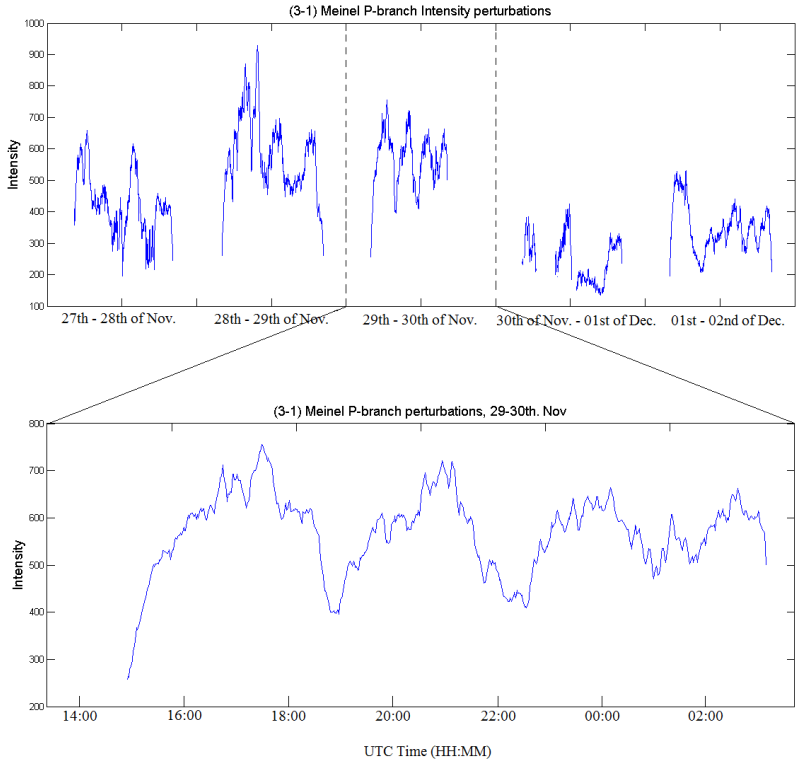

Figure 6.23: Intensity perturbations in the (3-1) Meinel P-branch, measured in Trondheim

To find the periods of oscillation in the OH layer, the Lomb-Scargle periodogram is used. This gives us the significant frequencies of $6.8 Day^{-1}$ with $\Delta f = 2.0 Day^{-1}$ and $13.7 Day^{-1}$ with $\Delta f = 1.6 Day^{-1}$. This gives the periods of 3.5h (3.0h, 4.0h) and 1.8h (1.7h, 1.9h).

6.1.7 Lower atmospheric winds

Figure 6.25 shows us lower atmospheric wind data for our 24 hour period. The data are collected by sounding balloons launched from Ørlandet($63.70°N, 9.60°E$). The blue line maps the wind speed at increasing altitudes, while the red arrows show the direction of the wind. In the way that the wind direction is plotted as the shaft of an arrow extending from the station toward the direction from which the wind is blowing.
The wind speeds are measured in knots (from 0 kts to ∼50kts). Converting them to m/s gives a scale from 0 m/s to 25.7 m/s. The altitude is given in units of kilofeet (kft), reaching 80 kft. This is equivalent to a height of ∼24.4 km.

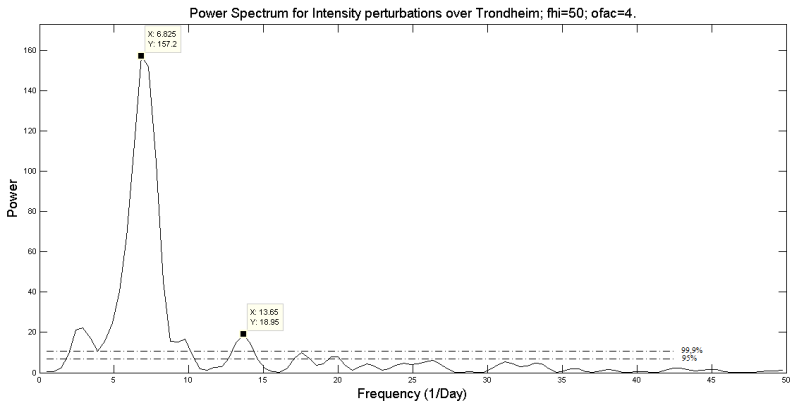

Figure 6.24: Normalized Lomb-Scargle periodogram for measurement over Trondheim the night between 29-30th.November

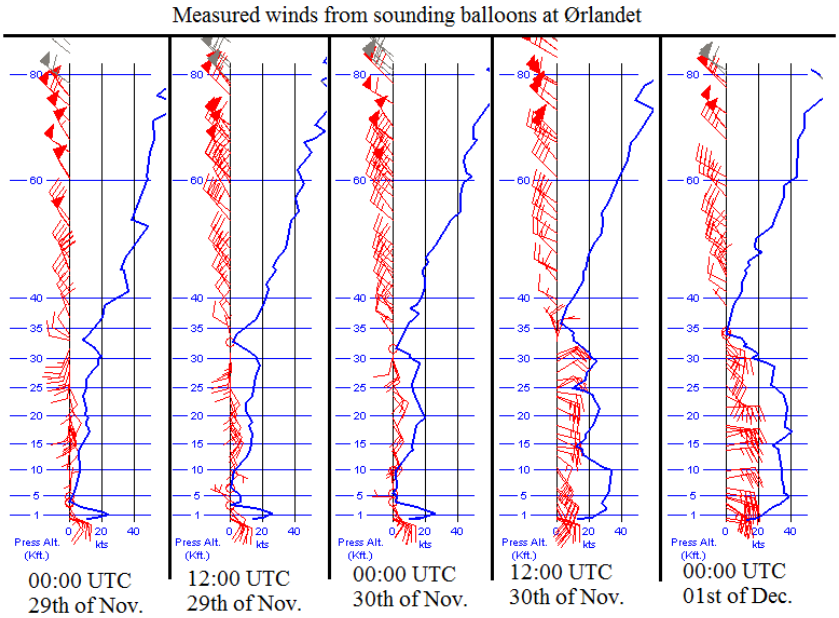

Figure 6.25: Lower atmospheric winds measured by sounding balloons at Ørlandet.

6.2 Andenes data

6.2.1 The five-night period (zonal analysis)

Removal of tidal waves

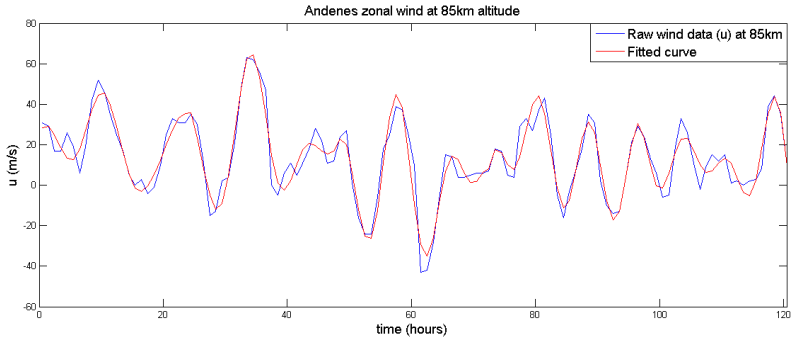

Figure 6.26: Raw zonal wind data from 85 km altitude (blue) plotted against its fitted curve (red).

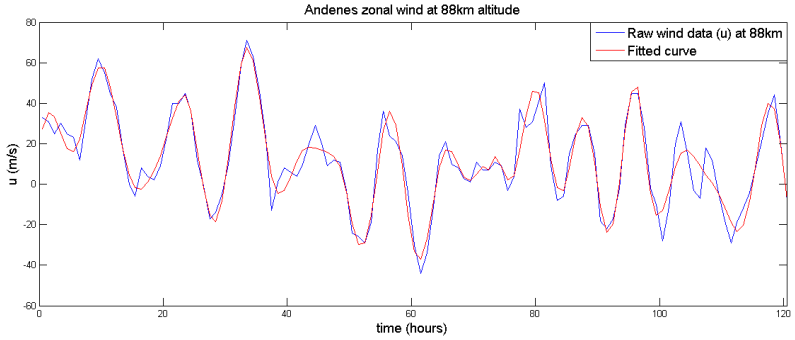

Figure 6.27: Raw zonal wind data from 88 km altitude (blue) plotted against its fitted curve (red).

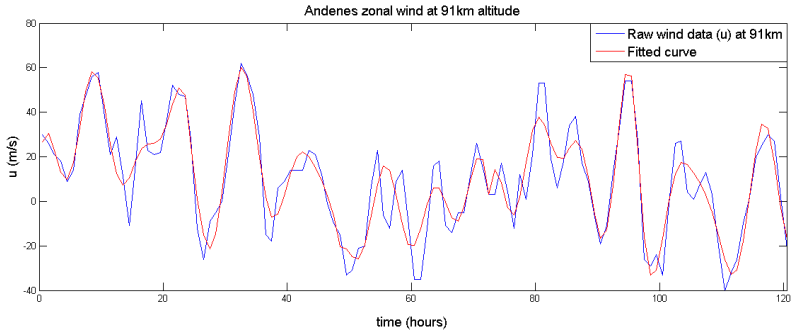

Figure 6.28: Raw zonal wind data from 91 km altitude (blue) plotted against its fitted curve (red).

Table of R^2 values:

		Dates				
		27-28th	28-29th	29-30th	30-01st	01-02nd
Altitudes	85km	0.8823	0.9096	0.9166	0.9029	0.7737
	88km	0.9222	0.9300	0.9210	0.8962	0.7938
	91km	0.7081	0.8664	0.5644	0.8591	0.8611

Table 6.3: Overview of R^2 values for the zonal winds over Andenes

Mean anomaly wind

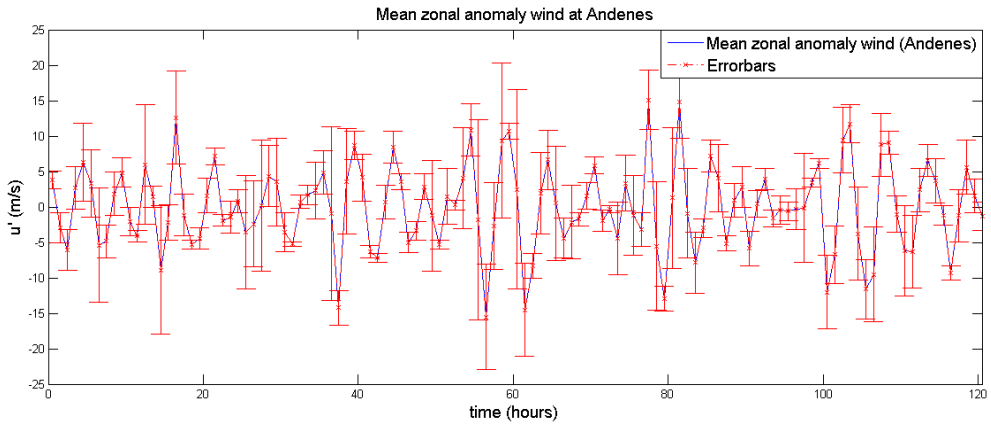

Figure 6.29: Mean zonal anomaly wind over Andenes, with errorbars.

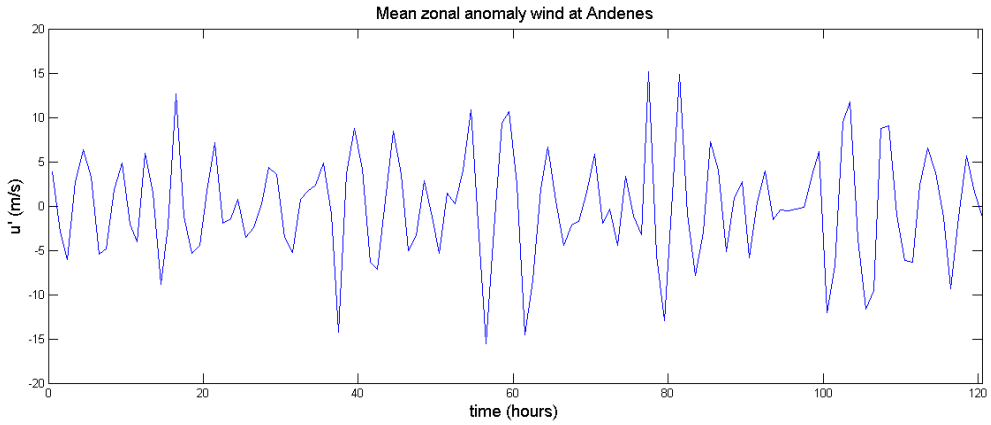

Figure 6.30: Mean zonal anomaly wind over Andenes.

The Fast Fourier Transform

In figure 6.31, three peaks are highlighted with a gaussian approximation to help find its FWHM. The first peak at frequency $0.19h^{-1}$ ($\Delta f = 0.017h^{-1}$) gives a period of 5.4h (5.1h, 5.6h). Then we got peaks of frequencies $0.22h^{-1}$ ($\Delta f = 0.020h^{-1}$) and $0.26h^{-1}$ ($\Delta f = 0.019h^{-1}$), giving periods of 4.6h (4.4h, 4.8h) and 3.8h (3.6h, 3.9h) respectively.

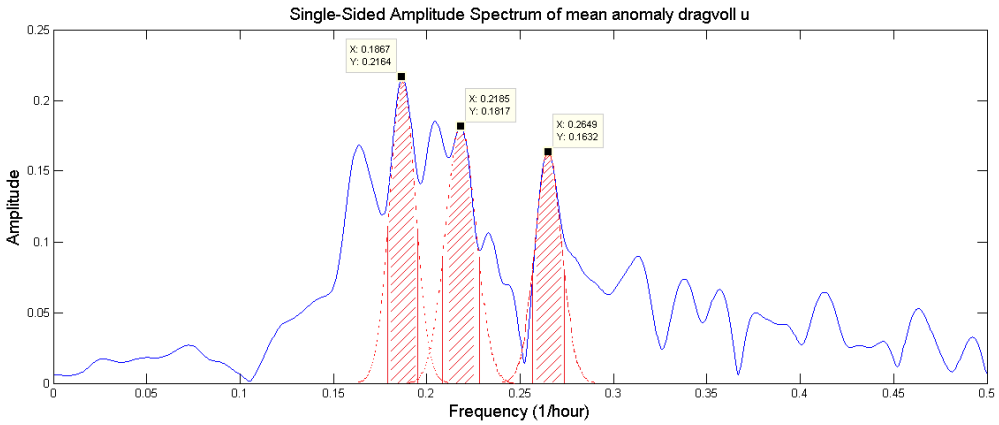

Figure 6.31: FFT of the mean zonal anomaly wind over Andenes.

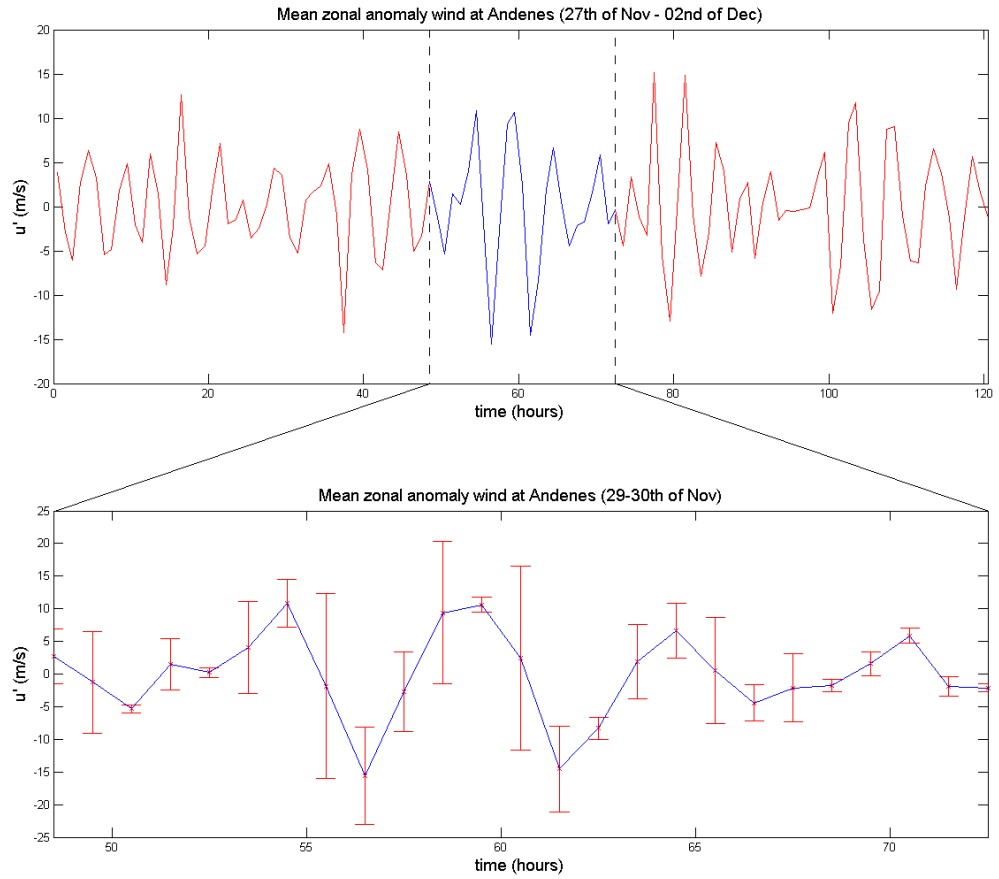

Figure 6.32: Transition from our five-night period to our night of interest, the 29-30th of November 2012, with errorbars.

6.2.2 The 24 hour period (zonal analysis)

The Fast Fourier Transform

One prominent peak of frequency $0.19h^{-1}$, with a FWHM of $0.11h^{-1}$. This gives us an period of 5.3h (4.1h, 7.3h)

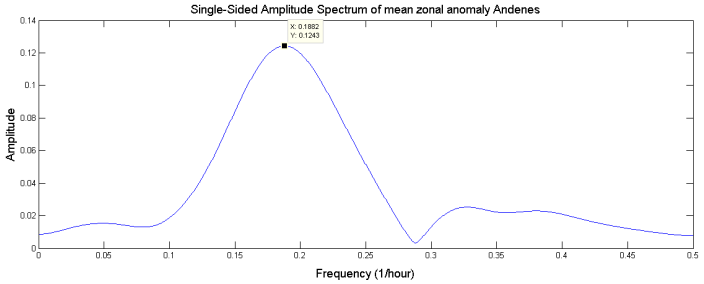

Figure 6.33: FFT of mean zonal anomaly wind during 29-30th of November over Andenes.

6.2.3 The five-night period (meridional analysis)

Removing tidal components

The following figures are important for the meridional analysis:

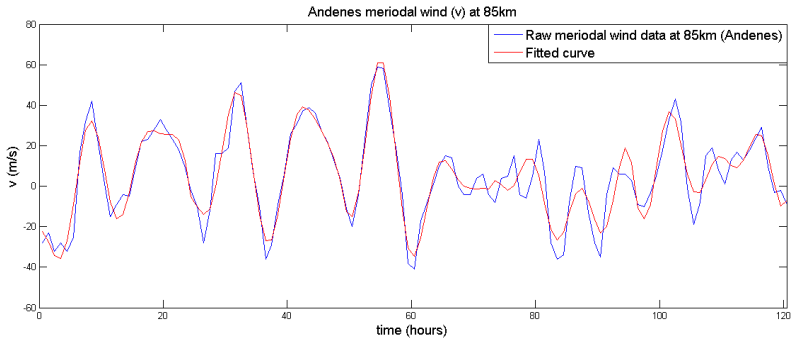

Figure 6.34: Raw meridional wind data from 85 km altitude (blue) plotted against its fitted curve (red).

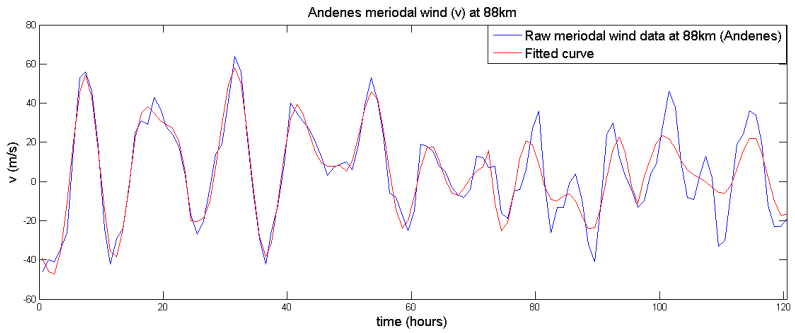

Figure 6.35: Raw meridional wind data from 88 km altitude (blue) plotted against its fitted curve (red).

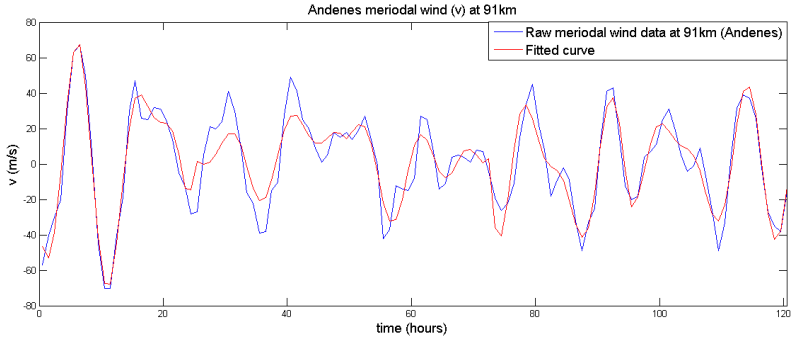

Figure 6.36: Raw meridional wind data from 91 km altitude (blue) plotted against its fitted curve (red).

Table of R^2 values:

		Dates				
		27-28th	28-29th	29-30th	30-01st	01-02nd
Altitudes	85km	0.9232	0.9388	0.9576	0.5593	0.7453
	88km	0.9665	0.9672	0.9155	0.6055	0.6209
	91km	0.9632	0.6800	0.7311	0.8840	0.8945

Table 6.4: Overview of R^2 values for the meriodal winds over Andenes

Mean anomaly wind

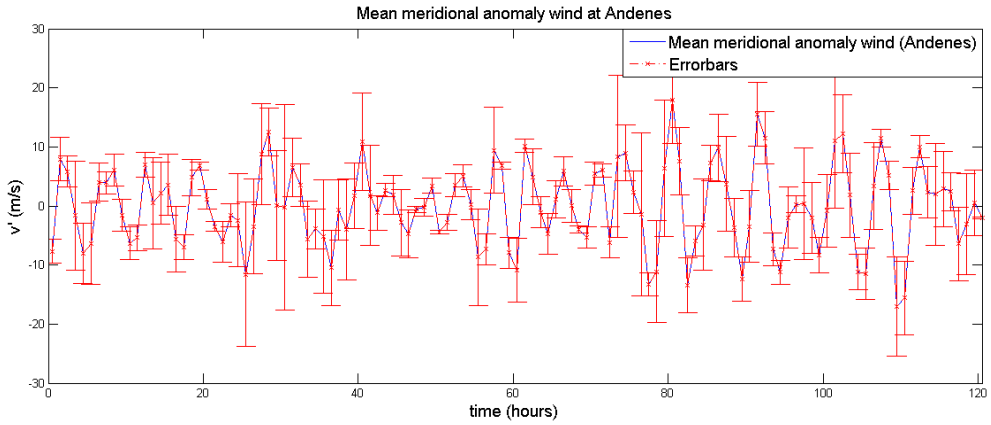

Figure 6.37: Mean meridional anomaly wind over Andenes, with errorbars.

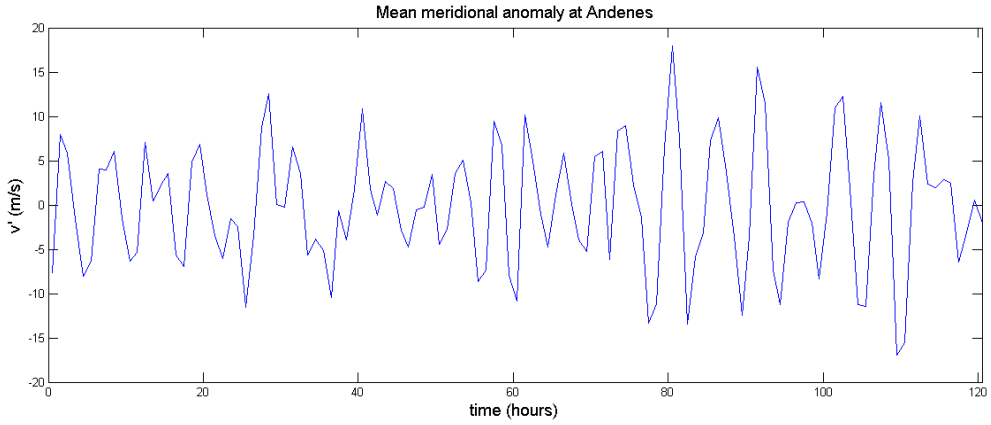

Figure 6.38: Mean meridional anomaly wind over Andenes.

The Fast Fourier Transform

In figure 6.39, two peaks of frequencies $0.18h^{-1}$ ($\Delta f = 0.029h^{-1}$) and $0.23h^{-1}$ ($\Delta f = 0.041h^{-1}$) are highlighted, giving periods of 5.6h (5.2h, 6.0h) and 4.3h (4.1h, 5.0h) respectively.

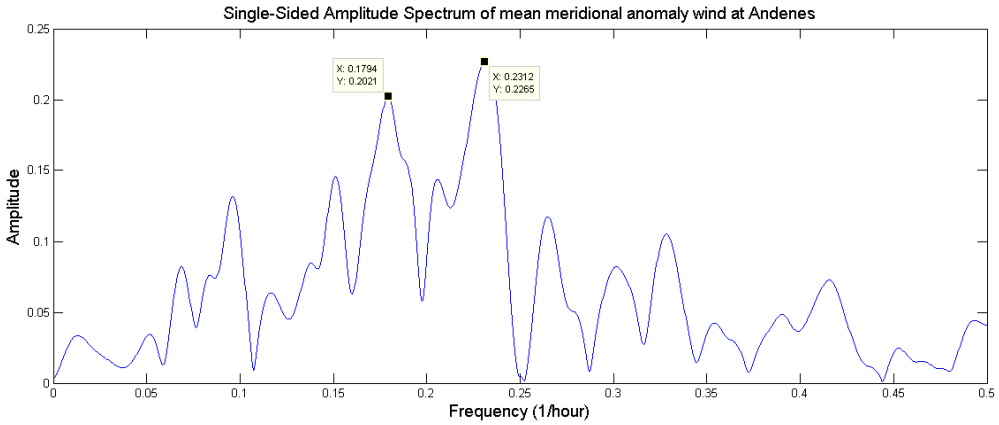

Figure 6.39: FFT of the mean meridional anomaly wind over Andenes.

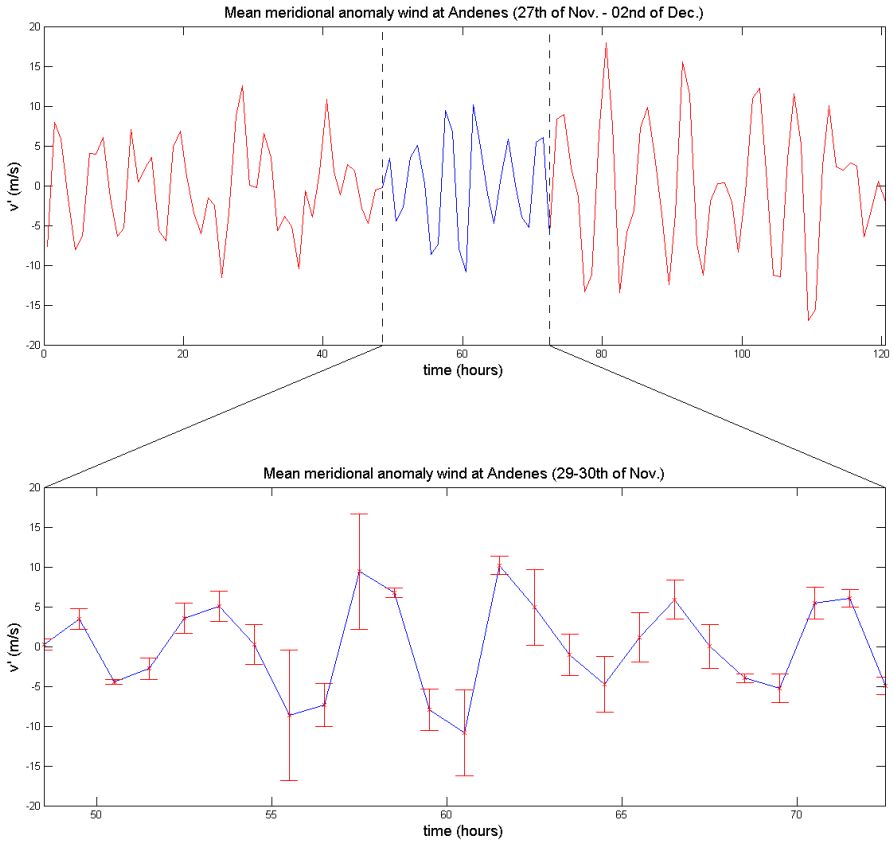

Figure 6.40: Transition from our five-night period to our night of interest, the 29-30th of November 2012, with errorbars.

6.2.4 The 24 hour period (meridional analysis)

The Fast Fourier Transform

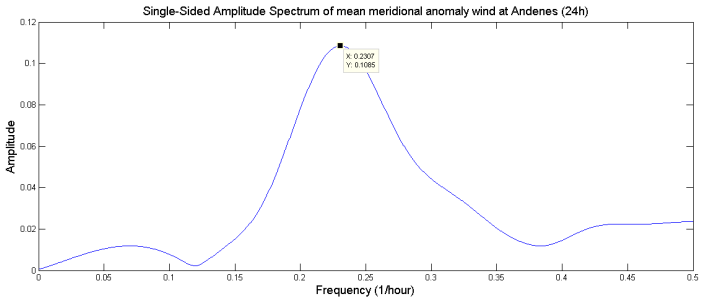

Figure 6.41: FFT of mean meridional anomaly wind during 29-30th of November over Andenes.

The period of Andenes mean meridional anamoly wind is given by the frequency peak in 6.41. A frequency of $0.23h^{-1}$ with $\Delta f = 0.10h^{-1}$ gives a period of 4.3h (3.5h, 5.4h).

6.2.5 Energy propagation

Figure 6.42 (and 6.43) shows contour plot of the cross-correlation function between the zonal (meridional) wind at 88 km and the zonal (meridional) winds at the different altitudes. Dark red colour indicates correlation, while dark blue colour indicates anti-correlation. Here, any positive (negative) lag tells us that the anomaly wind at that altitude lags (leads) the 88 km anomaly wind. The phase change between the altitudes are plotted in the right panel.

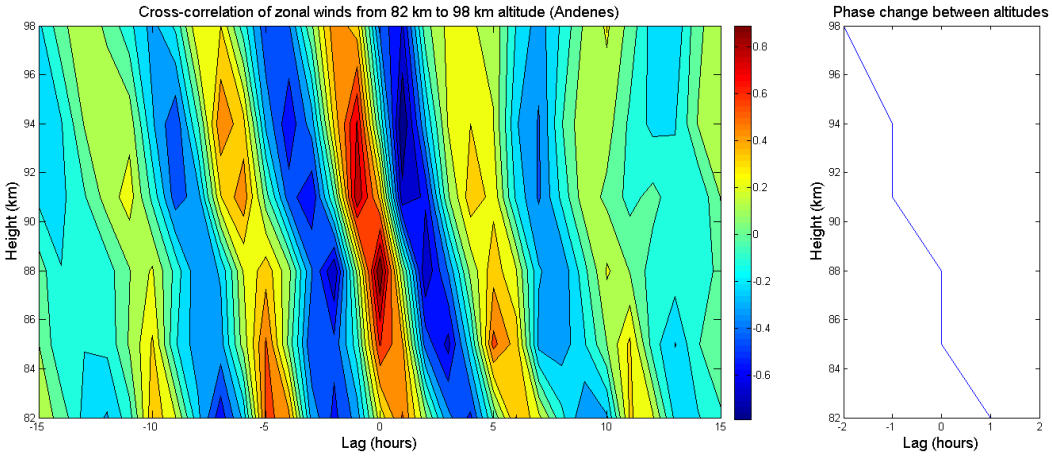

Figure 6.42: Left panel: Cross-correlation of zonal winds over Trondheim. All winds are correlated with the data extracted from the altitude of 88km. Red colour represents correlation and blue denotes anti-correlation. Right panel: vertical profile of phase change between zonal anomaly wind at 88 km altitude and zonal anomalies of different altitudes.

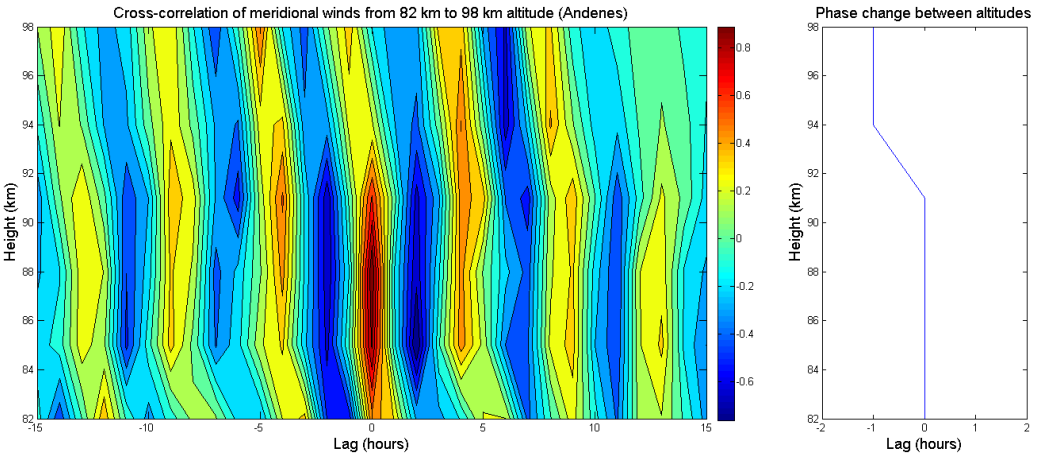

Figure 6.43: Left panel: Cross-correlation of meridional winds over Trondheim. All winds are correlated with the data extracted from the altitude of 88km. Red colour represents correlation and blue denotes anti-correlation. Right panel: vertical profile of phase change between meridional anomaly wind at 88 km altitude and meridional anomalies of different altitudes.

Figure 6.44 below shows the hodograph for the meridional and zonal anomaly wind perturbations at Andenes, 11:30 p.m. 29th of November 2012. The non-elliptical shape of the hodograph indicates that there are more than one frequency within the anomaly winds. However, its orientation is still clockwise which backs up the upward energy propagation given by the cross-correlation functions in figures 6.42 and 6.43.

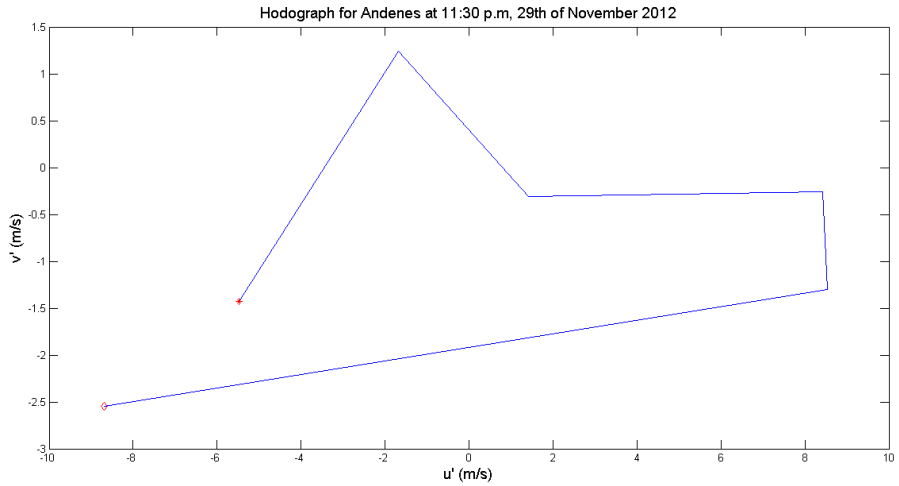

Figure 6.44: Andenes meridional anomaly wind perturbation plotted against the zonal anomaly wind perturbation. The red asterisk indicates the lowest altitude measurements; the red diamond indicates the highest altitude measurements.

6.2.6 Perturbations of the Hydroxyl Intensities

The following figure shows the intensity perturbations of the (3-1) Meinel P-branch, measured at Andenes.

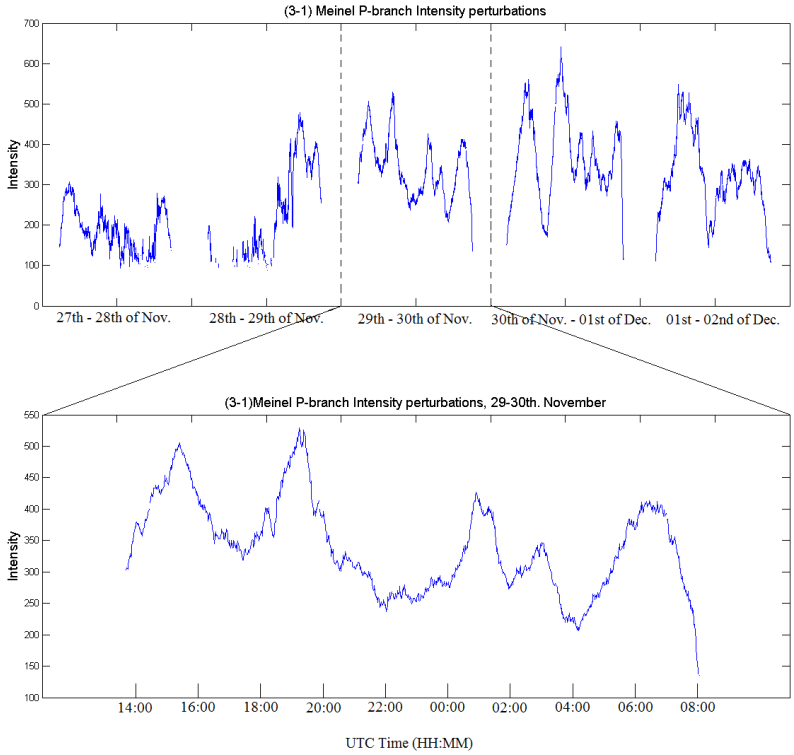

Figure 6.45: Intensity perturbations in the (3-1) Meinel P-branch, measured at Andenes

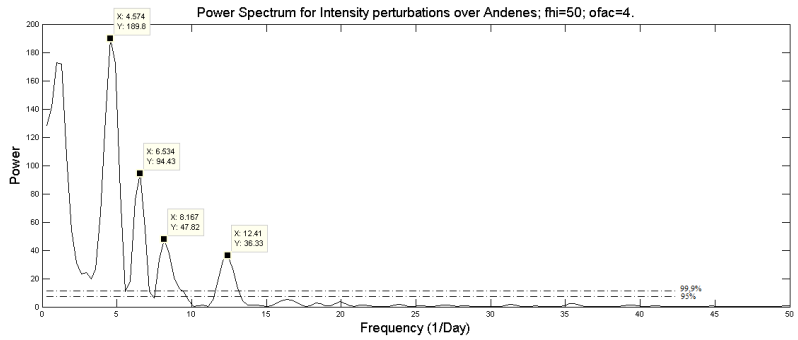

Figure 6.46: Normalized Lomb-Scargle periodogram for measurement over Andenes the night between 29-30th.November

6.2.7 Lower atmospheric winds

Figure 6.47 shows us lower atmospheric wind data for our 24 hour period at Bodø ($67.25°N, 14.40°E$).

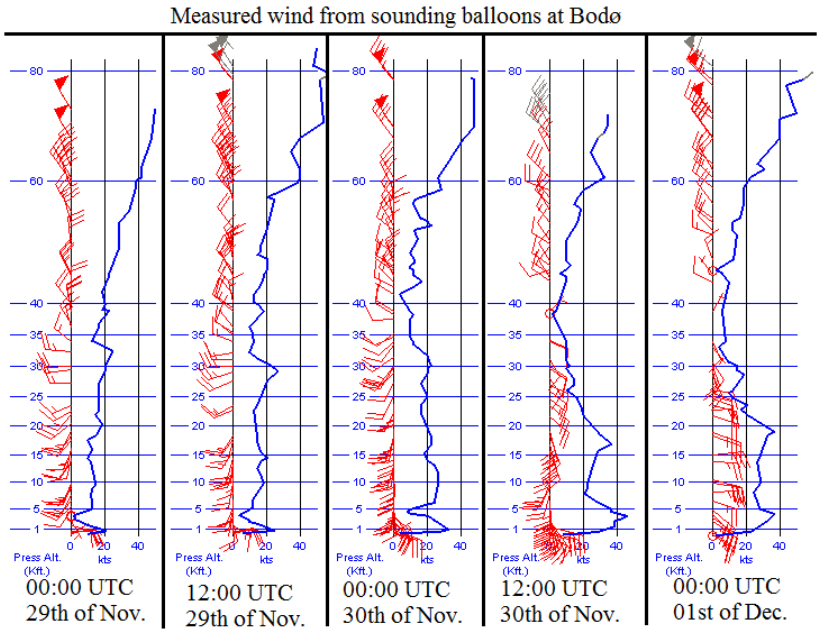

Figure 6.47: Lower atmospheric winds measured by sounding balloons at Bodø.

6.3 Correlation between the datasets

To say something about the correlation of the data collected from Andenes and Trondheim, the cross-correlation function ("crosscorr.m" in Matlab) is used. This function returns the normalized correlation of two datasets with a 95% confidence bound marked as a blue line.
To extract more information of any periodicity shared by the two sets of data, the FFT can be taken of the cross-correlation, to achieve a cross-spectrum. The cross-spectrum will have peaks at frequencies where oscillations appears at a fixed phase-relation between the two datasets.
Figures 6.48 to 6.51 below show both the cross-correlations and the cross-spectra of the mean anomalies at Andenes and Trondheim. We note that for each cross-correlation, we can see a significant correlation between the data. All of the cross-spectra will be furthered studied in the next chapter.

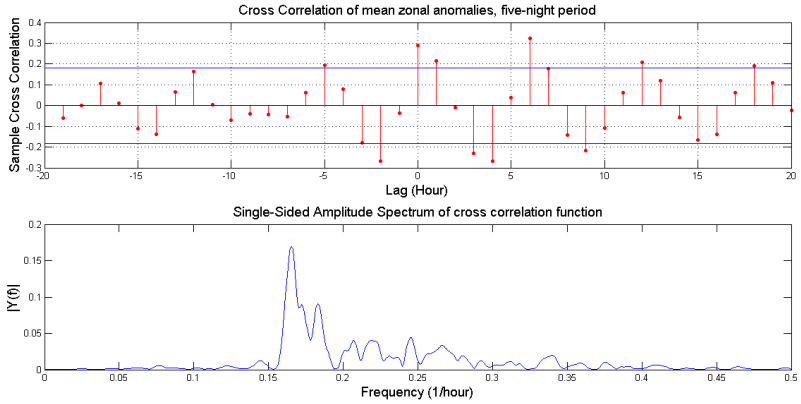

Figure 6.48: Upper plot: Cross correlation of mean zonal anomalies from Trondheim and Andenes during the five-night period. The blue constant values indicate the 95% confidence bounds. Lower plot: Corresponding cross spectrum.

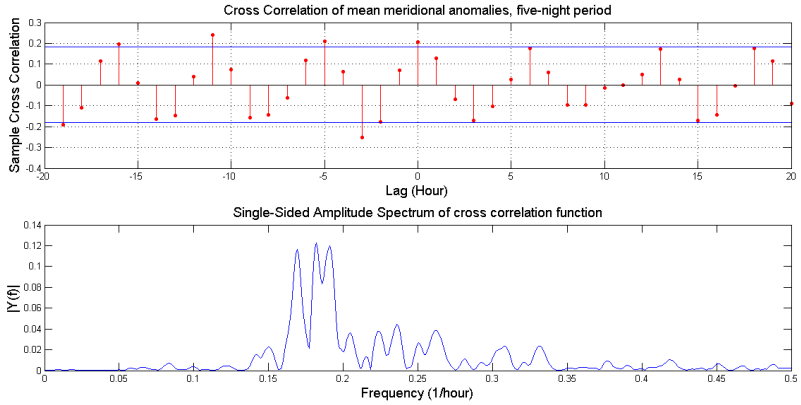

Figure 6.49: Upper plot: Cross correlation of mean meridional anomalies from Trondheim and Andenes during the five-night period. The blue constant values indicate the 95% confidence bounds. Lower plot: Corresponding cross spectrum.

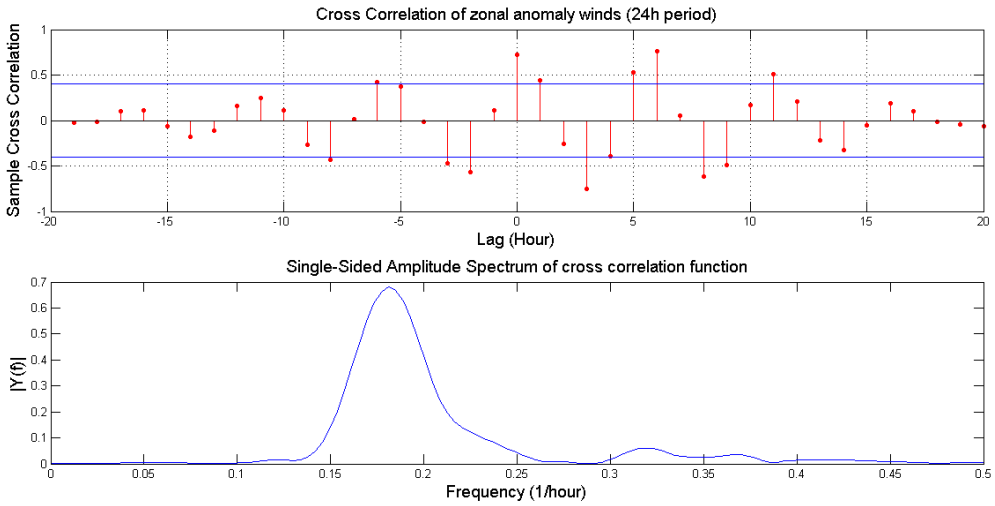

Figure 6.50: Upper plot: Cross correlation of mean zonal anomalies from Trondheim and Andenes during the twenty four hour period. The blue constant values indicate the 95% confidence bounds. Lower plot: Corresponding cross spectrum.

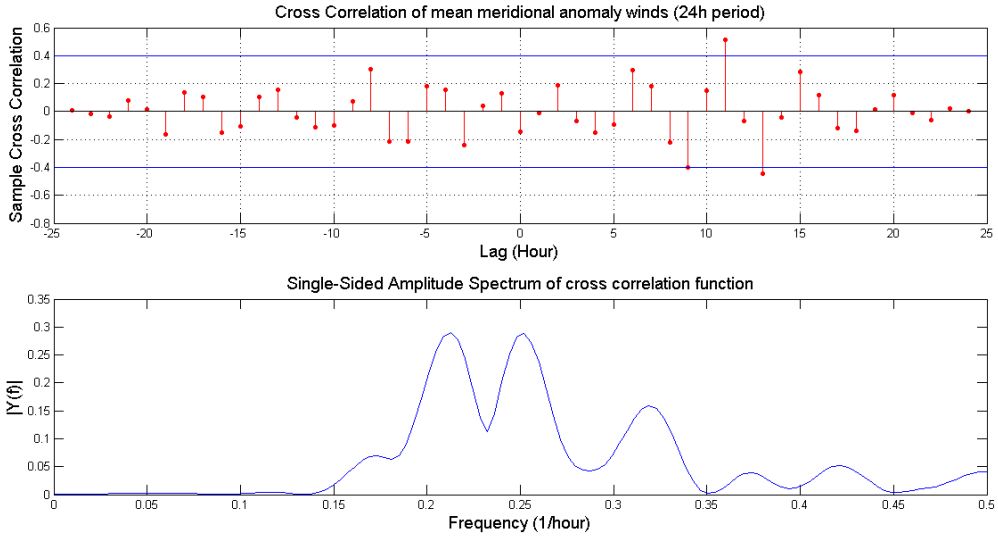

Figure 6.51: Upper plot: Cross correlation of mean meridional anomalies from Trondheim and Andenes during the five-night period. The blue constant values indicate the 95% confidence bounds. Lower plot: Corresponding cross spectrum.

Chapter 7

Discussion and Conclusion

Received data from the SKiYMET-radars at both Trondheim ($63.24°N, 10.27°E$) and Andenes ($69.17°N, 16.00°E$) are observed and analysed to examine the existence of a mesoscale gravity wave system present in the mesosphere. The datasets are subjected to the same analysis regarding removal of the tidal wave components and extraction of the frequencies present in the anomalies by fast fourier transforms. They were then run through a cross-correlation function, giving us information on whether or not the data are correlated. In this final chapter, the result obtained and presented in the previous chapter will be discussed and used to: 1. Reveal any mesoscale gravity wave system during the five-night period. 2. If any such system is found, suggest the most probable source.

1. Revealing any mesoscale system

Lets start with a visual comparison of the extracted mean anomaly winds. The next four figures show the zonal and mean anomalies from Andenes (red line) and Trondheim (blue line) plotted together in the same plot. The data from Andenes is shifted in the y-direction to get a better view of the oscillations occurring at each site. Keep in mind these data are collected at the same time, 700 km apart.

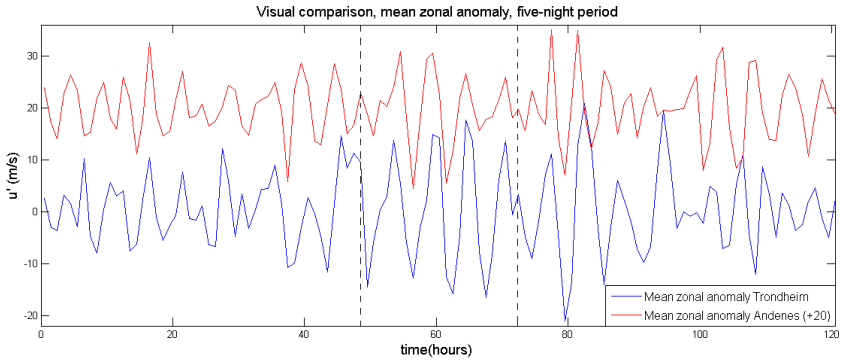

Figure 7.1: Visual comparison of the five-night mean zonal anomaly winds, for Trondheim (blue) and Andenes (red). (Andenes datapoints are shifted +20 units in the y-direction). The cross-correlation function for these data are given in figure 6.48.

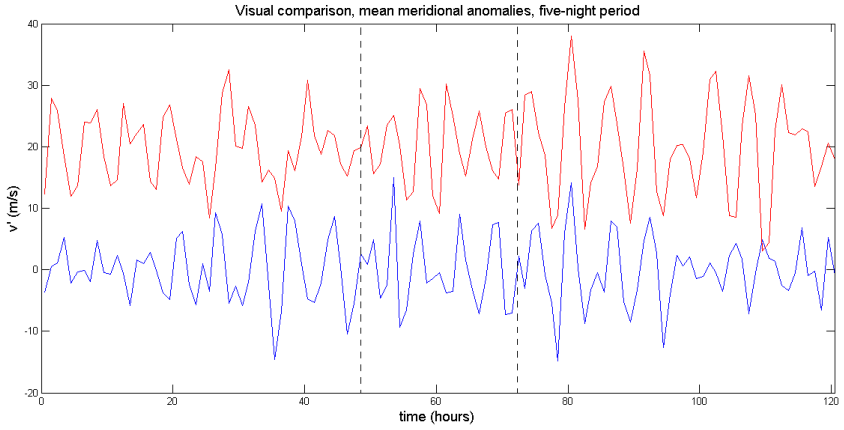

Figure 7.2: Visual comparison of the five-night mean meridional anomaly winds, for Trondheim (blue) and Andenes (red). (Andenes datapoints are shifted +20 units in the y-direction). The cross-correlation function for these data are given in figure 6.49.

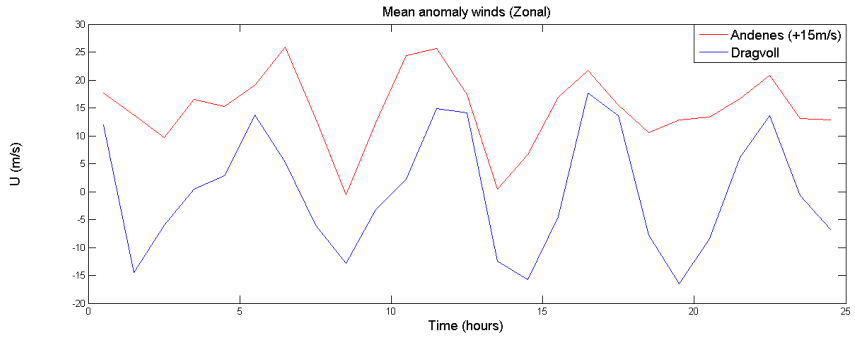

Figure 7.3: Visual comparison of the five-night mean zonal anomaly winds, for Trondheim (blue) and Andenes (red). (Andenes datapoints are shifted +20 units in the y-direction). The cross-correlation function for these data are given in figure 6.50.

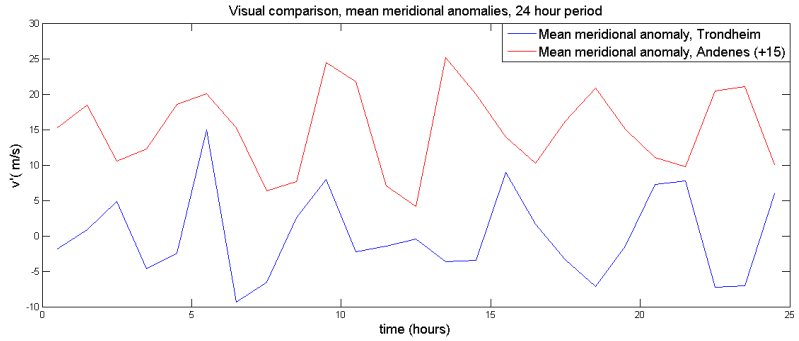

Figure 7.4: Visual comparison of the five-night mean meridional anomaly winds, for Trondheim (blue) and Andenes (red). (Andenes datapoints are shifted +20 units in the y-direction). The cross-correlation function for these data are given in figure 6.51.

The cross-correlation function ("crosscorr" in Matlab) gives us information regarding the correlation of the winds measured at the two stations. For both the five days period and the 24 hour period the result is a greater correlation between the mean zonal anomaly wind than for the mean meridional, nevertheless every cross-correlation function returns a significant correlation between the two datasets measured at Trondheim and Andenes. This strongly indicates that there is a mesoscale system of gravity waves which drives oscillations at both places simultaneous. The dominant period that are visible in the cross-correlation functions seems to be of $\sim$6 hours. To find other frequencies that are related between the two radar-sites and not just locally occurring, cross-spectra are obtained by taking FFT's of the cross-correlation functions.

Figure 7.5 shows us a comparison of the cross-spectrum versus the FFT for the mean zonal anomaly wind at Andenes and Trondheim during the five night period. The red lines marks frequency-peaks in the cross-spectrum, which indicates oscillations in the two datasets above that have a similar period and a fixed phase relationship with each other. The same comparison is made for the mean meridional anomaly winds, and for the anomalies during the 24 hour period. The result is shown below. The related periods of the marked peaks, with FWHM uncertainties are listed in the table in figure 7.9.

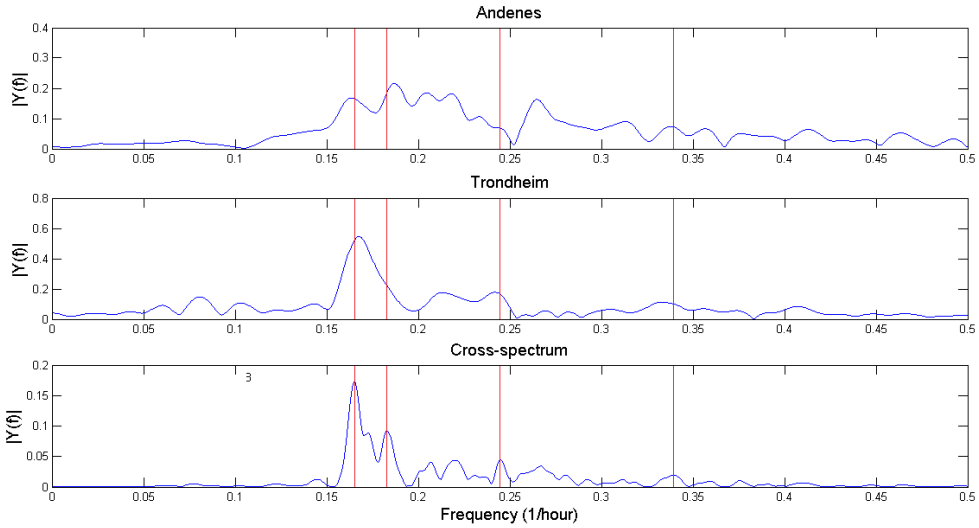

Figure 7.5: Upper plot: FFT of Andenes anomaly wind. Middle plot: FFT of Trondheim anomaly wind. Lower plot: Corresponding cross-spectrum. The data used are the mean zonal anomaly wind of the five-night period.

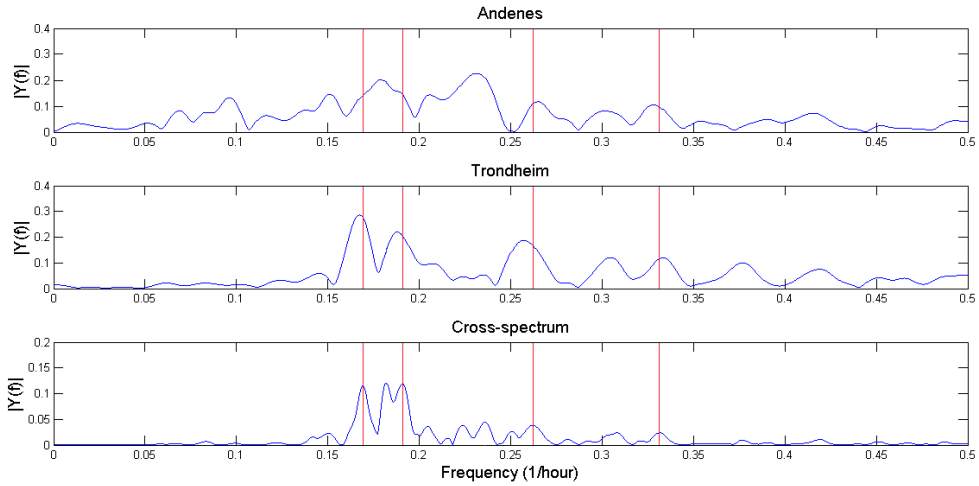

Figure 7.6: Upper plot: FFT of Andenes anomaly wind. Middle plot: FFT of Trondheim anomaly wind. Lower plot: Corresponding cross-spectrum. The data used are the mean meridional anomaly wind of the five-night period.

The table below (fig. 7.9) lists the frequency peaks highlighted by the red markers in fig. 7.5 - 7.8. These are the prominent peaks of the cross spectrum derived from each cross-correlation function. The purple columns indicates periods retrieved from the Lomb-Scargle analyses of the 24 hour intensity perturbation of the (3-1) Meinel band. The blank spots in the table are missing frequencies that do not show up as peaks in the FFT's of the related mean anomalies. There may be different reasons for this to happen. If two frequency peaks are close to each other, one may get "buried" by the other if the latter have a much bigger amplitude.

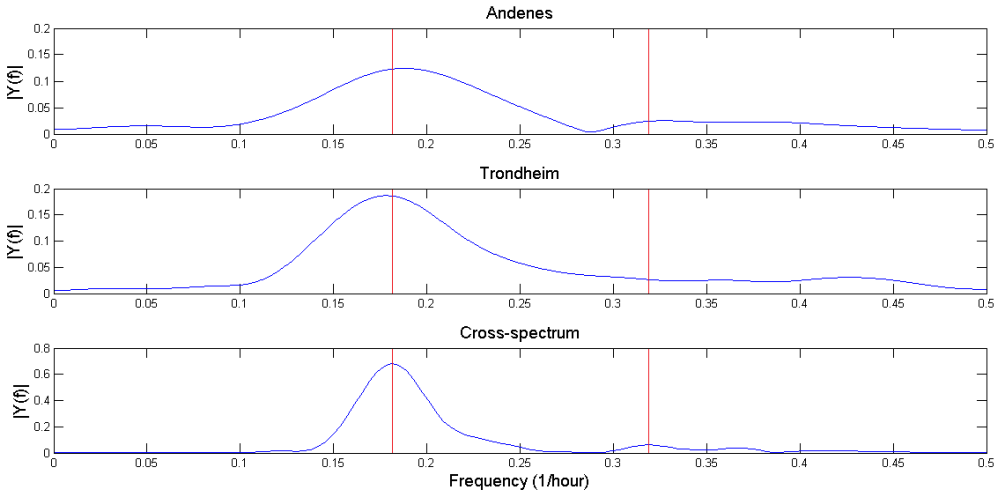

Figure 7.7: Upper plot: FFT of Andenes anomaly wind. Middle plot: FFT of Trondheim anomaly wind. Lower plot: Corresponding cross-spectrum. The data used are the mean zonal anomaly wind of the 24 hour period.

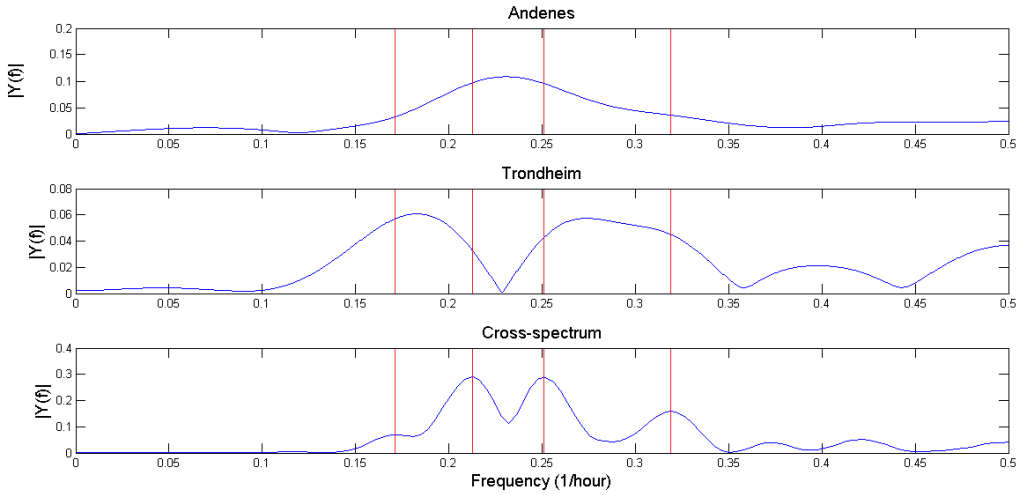

Figure 7.8: Upper plot: FFT of Andenes anomaly wind. Middle plot: FFT of Trondheim anomaly wind. Lower plot: Corresponding cross-spectrum. The data used are the mean meridional anomaly wind of the 24 hour period.

The highlighted green columns represents periods of ∼6 hours and ∼3 hours. These periods are consistent and clearly visible throughout the five night period, with the 6 hour oscillation being the dominant one (in accordance to the dominant period observed directly from the cross-correlation functions). This suggests that the large scale gravity waves were induced already prior to our night of interest.
The fact that these periods have a fixed phase relationship to each other is more evidence for the existence of a mesoscale gravity wave system. This leads the conclusion that indeed, we have a mesoscale gravity wave system that stretches 700 km from Trondheim to Andenes. The system apparently consists of a number of large scale waves, with

upward energy propagation and downward phase progression. The large scale waves that are apparent enough to be simultaneously identified at Andenes and Trondheim have periods of ∼6 and ∼3 hours.

		1st marker	2nd	3rd	4th
Five-night period	Zonal Andenes	6.1 h (5.7 h , 6.4h)	5.4 h (5.1 h, 5.6 h)		3.0 h (2.9 h, 3.0 h)
	Zonal Trondheim	6.0 h (5.6 h, 6.3 h)		4.1 h (4.0 h, 4.3 h)	3.0 h (2.9 h, 3.1 h)
	Zonal cross-spectrum	6.0 h (5.8 h, 6.2 h)	5.5 h (5.3 h, 5.6 h)	4.1 h (4.0 h, 4.1 h)	2.9 h (2.9 h, 3.0 h)
24 hour period	Zonal Andenes	5.3 h (4.1 h, 7.3 h)			3.0 h (2.7 h, 3.3 h)
	Zonal Trondheim	5.6 h (4.4 h, 7.3 h)			
	Zonal cross-spectrum	5.5 h (4.9 h, 6.3 h)			3.1 h (3.0 h, 3.3 h)
Five-night period	Meridional Andenes	5.6 h (5.2 h, 6.1 h)		3.8 h (3.7 h, 3.9 h)	3.0 h (2.9 h, 3.1 h)
	Meridional Trondheim	6.0 h (5.7 h, 6.3 h)	5.3 h (5.0 h, 5.5 h)	3.9 h (3.7 h, 4.0 h)	3.0 h (2.9 h, 3.1 h)
	Meridional cross-spectrum	5.9 h (5.8 h, 6.1 h)	5.3 h (5.1h, 5.5 h)	3.8 h (3.7 h, 3.9 h)	3.0 h (3.0 h, 3.0 h)
24 hour period	Meridional Andenes		4.3 h (3.5 h, 5.4 h)		
	Meridional Trondheim	5.5 h (4.7 h, 7.0 h)			3.1 h (2.9 h, 3.3 h)
	Meridional cross-spectrum	5.8 h (5.1 h, 6.5 h)	4.7 h (4.4 h, 5.1 h)	4.0 h (3.7 h, 4.2 h)	3.1 h (3.0 h, 3.3 h)
Hydroxyl perturbations	(3-1) Intensity Andenes		5.3 h (4.6 h, 5.9 h)	3.7 h (3.5 h, 4.0 h)	2.9 h (2.7 h, 3.1 h)
from Lomb-Scargle	(3-1) Intensity Trondheim				3.5 h (3.0 h, 4.0 h)

Figure 7.9: Table showing frequencies highlighted by red markers in fig. 7.5 - 7.8.

Since we only are able to measure OH airglow perturbations during night time (relative short periods of time), it can be slightly difficult to detect the longer period waves with the spectrograph. Figure 6.45 shows the length of the measurement done during the night of 29th - 30th of November to be 18 hours. They were able to detect longer period oscillations than Trondheim (fig. 6.23), which only measured for 12 hours. Also, clouds may interact with the data collection of airglow perturbation, and might destroy the wave signature. This effect can be seen during the night between the 30th and 01st of December in Trondheim (fig. 6.23), and the night between the 27th-28th and 28th - 29th at Andenes (fig. 6.45). However, the spectrographs are both able to detect a ∼3 hour periodic oscillation occurring at our night of interest.

2. Suggesting the most probable source

For mesoscale gravity wave systems to arise, one needs a mesoscale source to induce the large waves. The scandinavian mountain range illustrated in figure 2.7, could be a suitable source of origin, if the conditions are right. For a freely propagating mesoscale mountain wave to be induced, one would need strong winds ($\sim$10 m/s) to blow (close to) perpendicular over the mountains across the mountain range. To check whether these parameters were present somewhere between the 27th. of November and the 02nd. of December, balloon soundings were collected from Ørlandet and Bodø (figures 6.25 and 6.47). The mapping of the lower atmospheric winds tells us that they are neither directed perpendicular onto the mountain range (going northwards from Ørlandet and Bodø), nor do they have the strength necessary to induce mountain waves (close to zero m/s at Ørlandet and merely 5 m/s at Bodø, at 1500 meters altitude). The hypothesis regarding the scandinavian mountain range to be the source of origin must therefore be rejected.

One does not need to look too far for other sources. By studying the balloon soundings further, one can spot what seems to be a very large frontal system moving in over the country. At Ørlandet we see the winds are directed northwards (north-west) up to an altitude of 9 km, where it drastically turn 180 degrees and starts to flow south-east at higher altitudes. The same happens at Bodø. As discussed in the theory chapter, these front waves can represent a corrugated surface (as a mountain range) and therefore induce gravity waves. In general, airflow will also create a wind shear, and the highly variable eddies created in the shear can easily launch freely propagating waves. It seems like the frontal wave system hits Ørlandet and Bodø almost simultaneously. It may have originated offshore, thus explaining why the mesoscale gravity wave system are apparent throughout the five-night period.

Further work

For further work, one may want to identify the orientation of the mesoscale gravity wave system. This can be done if the wave system is observable (with balloon soundings and a SKiYMET-radar) at the Esrange space center in Sweden. If the mean anomalies were found to correlate with the data from Andenes and Trondheim, one can triangulate the wave, mapping its orientation and horizontal wavelength.

Another task would be to include a modelling component, for example the WACCM model which can model atmospheric phenomenons to a height of 150 km. This model could use the balloon sounding data to detect and simulate the frontal or shear waves, and generate the gravity waves induced by this system.

Bibliography

Andrews, D. G. (2010). *An Introduction to Atmospheric physics*. Cambridge University press, second edition edition.

Berge, F. T. (2011). Development of a spectrometer system to remotely sense mesospheric temperature. Master's thesis, Norwegian University of Science and Technology.

Ekern, K. L. (2013). Climatology of short-period tidal oscillations in the upper atmosphere. Master's thesis, Norwegian University of Science and Technology.

Genesis Software. Skiymet meteor radar.

Girod, B., Rabenstein, R., and Stenger, A. (2001). *Signals and Systems*. John Wiley and Sons, Ltd, first edition edition.

Glynn, E. F., Chen, J., and Mushegian, A. R. (2006). Detecting periodic patterns in unevenly spaced gene expression time series using lomb–scargle periodograms. *Oxford Journals, Bioinformatics*, 22.

Hall, G. E., Meek, C. E., and Manson, A. H. (1995). Hodograph analysis of mesopause region winds observed by three mf radars in the canadian prairies. *Journal of Geophysical research*, 100.

Hennum, E. A. (2013). A new algorithm for remote sensing mesopause temperatures using the hydroxyl airglow. Master's thesis, Norwegian University of Science and Technology.

Hibbins, R. E., Espy, P. J., Jarvis, M. J., Riggin, D. M., and Fritts, D. C. (2007). A climatology of tides and gravity wave variance in the mlt above rothera, antarctica obtained by mf radar. *Journal of Atmospheric and Solar-Terrestrial Physics*, 69.

Hocking, W. K. (2001). Buoyancy (gravity) waves in the atmosphere.

Leibniz-Institut für atmosphären physik. The andenes meteorradar.

Lin, Y.-L. (2007). *Mesoscale Dynamics*. Cambridge University press, first edition edition.

Lindsey, R. (2009). Climate and earth's energy budget.

Liu, A. Z. and Swenson, G. R. (2002). A modeling study of o_2 and oh perturbations induced by atmospheric gravity waves. *Journal of Geophysical research*, 108.

Moffat-Griffin, T., Hibbins, R. E., Jarvis, M. J., and Colwell, S. R. (2011). Seasonal variations of gravity wave activity in the lower stratosphere over an antarctic peninsula station. *Journal of Geophysical research*, 116.

Press, W. H., Teukolsky, S. A., Vetterling, W. T., and Flannerly, B. P. (1992). *Numerical Recipes in C - The Art of Scientific Computing.* Cambridge University Press, The Pitt Building, Trumpington Street, Cambridge, 2 edition edition.

Salby, M. L. (1996). *Fundamentals of Atmospheric Physics.* Academic press, San Diego, first edition edition.

Walterscheid, R. and Vincent, N. (1996). Tidal generation of the phase-locked 2-day wave in the southern hemisphere summer by wave-wave interactions. *Journal of Geophysical research*, 101.

Wayne, R. P. (1985). Chemistry of atmospheres.